Tellus SERIES A DYNAMIC METEOROLOGY AND OCEANOGRAPHY
PUBLISHED BY THE INTERNATIONAL METEOROLOGICAL INSTITUTE IN STOCKHOLM

Effect of lateral boundary perturbations on the breeding method and the local ensemble transform Kalman filter for mesoscale ensemble prediction

By KAZUO SAITO[1]*, HIROMU SEKO[1], MASARU KUNII[1] and TAKEMASA MIYOSHI[2],
[1]*Meteorological Research Institute, 1-1 Nagamine, Tsukuba, Ibaraki 305-0052, Japan*;
[2]*University of Maryland, College Park, MD 20742, USA*

(Manuscript received 18 February 2011; in final form 11 October 2011)

ABSTRACT

The effect of lateral boundary perturbations (LBPs) on the mesoscale breeding (MBD) method and the local ensemble transform Kalman filter (LETKF) as the initial perturbations generators for mesoscale ensemble prediction systems (EPSs) was examined. A LBPs method using the Japan Meteorological Agency's (JMA's) operational one-week global ensemble prediction was developed and applied to the mesoscale EPS of the Meteorological Research Institute for the World Weather Research Programme, Beijing 2008 Olympics Research and Development Project. The amplitude of the LBPs was adjusted based on the ensemble spread statistics considering the difference of the forecast times of the JMA's one-week EPS and the associated breeding/ensemble Kalman filter (EnKF) cycles. LBPs in the ensemble forecast increase the ensemble spread and improve the accuracy of the ensemble mean forecast. In the MBD method, if LBPs were introduced in its breeding cycles, the growth rate of the generated bred vectors is increased, and the ensemble spread and the root mean square errors (RMSEs) of the ensemble mean are further improved in the ensemble forecast. With LBPs in the breeding cycles, positional correspondences to the meteorological disturbances and the orthogonality of the bred vectors are improved. Brier Skill Scores (BSSs) also showed a remarkable effect of LBPs in the breeding cycles. LBPs showed a similar effect with the LETKF. If LBPs were introduced in the EnKF data assimilation cycles, the ensemble spread, ensemble mean accuracy, and BSSs for precipitation were improved, although the relative advantage of LETKF as the initial perturbations generator against MDB was not necessarily clear. LBPs in the EnKF cycles contribute not to the orthogonalisation but to prevent the underestimation of the forecast error near the lateral boundary.

The accuracy of the LETKF analyses was compared with that of the mesoscale 4D-VAR analyses. With LBPs in the LETKF cycles, the RMSEs of the forecasts from the LETKF analysis were improved and some of them became comparable to those of the mesoscale 4D-VAR analyses based on the JMA's operational data assimilation system. These results show the importance of LBPs in the MBD method and LETKF. LBPs are critical not only to ameliorate the underestimation of the ensemble spread in the ensemble forecast but also to produce better initial perturbations and to improve the LETKF analysis.

Keywords: ensemble Kalman filter, breeding, boundary perturbation, ensemble prediction, B08RDP

1. Introduction

The operational numerical weather prediction (NWP) has been considerably improved by continuous advance in numerical modelling and data assimilation techniques. However, many difficulties remain in predicting mesoscale severe weather with specifications of intensity, location and timing. One of the reasons for these difficulties is the general lack of observation data for high-resolution real-time data assimilation. Another reason is the inherent low predictability of small-scale severe phenomena that occur under convectively unstable atmospheric conditions.

To cope with significant forecast uncertainties of mesoscale severe weather, the mesoscale ensemble prediction system (EPS) is becoming viable. Operations of short-range regional EPSs have been started in some forecast centers: the Short-Range Ensemble Forecast (SREF) system of the

*Corresponding author.
email: ksaito@mri-jma.go.jp

Citation: Tellus A 2012, **64**, 11594, DOI: 10.3402/tellusa.v64i0.11594

National Center for Environment Prediction (NCEP) (Du et al., 2003), the Met Office Global and Regional Ensemble Prediction System (MOGREPS) of the UK Met Office (Bowler et al., 2008), the Limited Area Ensemble Prediction System within the COSMO consortium (COSMO-LEPS) of Agenzia Regionale Prevenzione e Ambiennte -Romagna (ARPA-SMR) of Italy (Marsigli et al., 2005) and the Limited Area Ensemble Forecasting system using the ALADIN model (ALDIN-LAEF) of the Central Institute for Meteorology and Geodynamics (ZAMG) of Austria (Wang et al., 2011). One of the possible choices for the initial perturbation method for a limited model EPS is dynamical downscaling of a global EPS. Some current operational regional EPSs use downscaling of perturbations produced by the global EPS (Marsigli et al., 2005; Houtekamer et al., 2007; Bowler et al., 2008), whereas others generate initial perturbations using a regional model-based perturbation method such as the Breeding of Growing Modes (BGM) method (e.g. Du et al., 2003; Wang et al., 2011). Recently, the use of the ensemble transform Kalman filter (ETKF; Bishop et al., 2001) as the generator of initial perturbations for global EPSs has become more frequent. Wang and Bishop (2003) compared BGM and ETKF as initial perturbations generators and showed that ETKF had the advantage that the amplitude of the initial perturbations reflected the magnitude of the local analysis error. However, they used a low-resolution (T42 with 18 vertical levels) global climate model for the comparison. Bowler (2006) compared ensemble prediction among singular vector (SV), BGM and ETKF methods, but the model was a toy model (Lorenz model; Lorenz, 1995). Bowler and Mylne (2009) tested ETKF as the initial perturbations generator for a regional version of MOGREPS, but because the mesoscale ETKF did not yield clear advantage, the operational system was implemented with global ETKF downscaling (Bowler et al., 2008). They did not compare regional ETKF with regional BGM.

In addition to the choice of initial perturbations, another important feature of mesoscale EPSs is the existence of lateral boundary conditions (LBCs). As shown by Anthes et al. (1985, 1989), LBCs play a key role in limited-area NWP. Because error growth in a mesoscale model is restricted by the LBCs (Errico and Baumhefner, 1987; Warner et al., 1989), an ensemble forecast in a limited-area model tends to lose its variance as lead time increases if the LBCs are not perturbed (Hamill and Colucci, 1997; Hou et al., 2001). Nutter et al. (2004a, 2004b) examined the impact of coarsely resolved and temporally interpolated LBCs on the dispersion of limited-area model ensemble forecasts and showed that the lateral boundary perturbations (LBPs) help to increase the ensemble spread of the nested model. A barotropic periodic channel domain model was used in their study. Recently, Saito et al. (2010b) applied LBPs from the global one-week EPS forecast of the Japan Meteorological Agency (JMA) to their ensemble prediction of the Myanmar cyclone Nargis and showed that when LBPs were introduced, the ensemble spread increased by about 50% and root mean square errors (RMSEs) of the ensemble mean forecast became smaller than the case without LBPs.

Those previous studies have shown the importance of LBPs in mesoscale ensemble forecasts. However, some initial perturbations generators such as the BGM and the Ensemble Kalman filter (EnKF) methods need LBCs in their breeding/EnKF cycles, and their effects on the produced initial perturbations have hardly been investigated. Torn et al. (2006) was the first to assess how LBCs affect the performance of limited-area EnKFs. They applied two methods, LBPs provided by a larger domain and a simpler alternative method employing presumed spatial and temporal covariance relationships to an EPS using the Weather Research and Forecasting (WRF) model (Skamarock et al., 2005) and suggested that ensemble LBCs can be specified without a global ensemble by perturbing around an ensemble mean. However, the horizontal resolution of the regional ensemble in their study was 100 km, which is very coarse for current mesoscale EPSs. Moreover, they did not compare the methods using the global ensemble perturbations. Recently, Vié et al. (2011) studied the impact of uncertainties on initial and LBCs in cloud-resolving ensemble simulations with a mesoscale model and showed that LBPs have an impact at longer range to increase the ensemble spread. However, the uncertainty on LBCs was not considered in the perturbed observations experiment to generate the initial perturbations.

In 2008, the World Weather Research Programme (WWRP) Beijing 2008 Olympics Forecast Demonstration/Research and Development Project (B08FDP/RDP) was conducted in conjunction with the Beijing Olympic Games. B08FDP/RDP was an international research project of WWRP of the World Meteorological Organization (WMO) for short-range weather forecasting. The main part of the B08RDP project, called Tier-1, was an intercomparison of mesoscale EPSs with a horizontal resolution of 15 km. The Meteorological Research Institute (MRI) of JMA participated in this project by applying the JMA nonhydrostatic model (NHM). Prior to the 2008 intercomparison experiment of B08RDP, MRI developed five initial perturbation methods and compared their performances objectively: (1) a downscaling method of JMA's operational one-week EPS, (2) a targeted global model SV method, (3) a mesoscale model SV method, (4) a mesoscale BGM method, and (5) an ensemble transform method based on the local ensemble transform Kalman filter (LETKF). In addition, MRI developed two LBP methods and examined their impacts on the ensemble forecast.

The results of the comparison of the five initial perturbation methods for the mesoscale ensemble prediction conducted by MRI are reported in a separate paper (Saito et al., 2011; hereafter referred as 'S2011'). As the second part of the MRI/JMA studies for the B08RDP project, we examined the influence of LBPs on mesoscale EPSs. Because the importance of LBPs in mesoscale EPSs was already made clear by the previous studies, we focus here on how LBPs affect the performance of BGM and LETKF as the initial perturbation generators by investigating their effect on the breeding/EnKF cycles. EPS performance is validated by the RMSEs of the ensemble forecasts, the ensemble spreads and their growth rate and Brier Skill Scores (BSSs) for precipitation. Moreover, the accuracy of the LETKF analyses as a data assimilation method with and without LBPs in the EnKF cycles is compared with that of state-of-the-art mesoscale 4D-VAR analyses (Kunii et al., 2010).

This article is organised as follows. Section 2 briefly introduces the WWRP B08FDP/RDP project. Section 3 presents the initial and LBPmethods used in the study. Section 4 describes the design of the experiment. In Section 5, the pure effect of LBPs on the EPS with no initial perturbations is reconfirmed, and then the effect of the LBPs on the BGM method is presented. In Section 6, the effect of LBPs in the EnKF cycles of LETKF is presented. In Section 7, we discuss the evolution of the energy norm, and the BSSs of the ensemble experiments, and we perform a similarity index analysis to evaluate the characteristics of the bred perturbation vectors. In addition, the accuracy of the LETKF analyses is compared with that of the mesoscale 4D-VAR analyses. Summary and concluding remarks are given in Section 8.

2. The WWRP B08FDP/RDP project

The B08FDP/RDP was an international research project of WWRP that succeeded the Sydney 2000 Forecast Demonstration Project (Sydney 2000FDP; Keenan et al., 2003). The B08FDP/RDP consisted of two components: an FDP component for very short-range forecasting of up to 6 h based on nowcasting, and an RDP component for short-range forecasts of up to 36 h based on mesoscale EPSs. A main part of the RDP component was the intercomparison of mesoscale EPSs based on regional models with a horizontal resolution of 15 km, called Tier-1.

The 2008 B08RDP experiment was conducted over about one month in summer 2008 to coincide with the period of the Beijing Olympic Games that took place from 8 to 24 August 2008. In the Tier-1 ensemble experiment, the six participants[1] were requested to run their ensemble predictions for a forecast time (FT) of up to 36 h, starting every day at 12 UTC. The results were interpolated into verification grids with a resolution of 0.15° over a common verification domain (105–125°E, 30–45°N; see Fig. 4). Duan et al. (2012) provided a detailed overview of B08RDP, and Kunii et al. (2011) have reported the results of the international EPS intercomparison.

Prior to the 2008 intercomparison experiment of B08RDP, MRI developed five initial perturbation methods and two LBP methods and examined their performance and impacts on the ensemble forecast. Details of MRI and JMA's activities in B08FDP/RDP have been published as an MRI Technical Report (Saito et al., 2010a), while the results of the comparison of the five initial perturbation methods have been reported in S2011.

3. Initial and LBP methods

3.1. Initial perturbation methods

In this study, we compare two initial perturbation methods, the mesoscale breeding (MBD) method and the LETKF method with and without the LBPs.

3.1.1. MBD method. MBD employs a self-breeding cycle with NHM. To evaluate the magnitude of the bred perturbations, the moist total energy (TE) norm of Barkmeijer et al. (2001) was employed:

$$TE = \frac{1}{2}\left\{\iint (U-\overline{U})^2+(V-\overline{V})^2+\frac{c_p}{\Theta}(\theta-\overline{\theta})^2+w_q\frac{L^2}{c_p\Theta}(q-\overline{q})^2\right\}\mathrm{d}S\mathrm{d}P + \frac{1}{2}\int\frac{R\Theta}{P_r}(P_{sea}-\overline{P_{sea}})^2 dS. \quad (1)$$

Here, overbar represents the ensemble mean. According to the JMA global EPS, $\Theta = 300\,\mathrm{K}$, $P_r = 800\,\mathrm{hPa}$ and $w_q = 0.1$ were used, and the norm was computed below 5.3 km above ground level.

To produce bred vectors, 6-h self-breeding cycles at a horizontal resolution of 40 km were performed (Fig. 1a). The moist TE norms were computed by the differences between the control runs and the perturbed runs, and the bred perturbations of all prognostic variables except soil temperature were normalised every 6 h. The normalisation coefficients were determined by the square root of the ratios of the moist TE norms of perturbed runs to a standard norm, which was computed using the prescribed values of the model variables (0.35 hPa for mean sea level pressure, 1.0 m/s for wind speed, 0.4 K for potential temperature and 5% for relative humidity (RH), respectively). These values are about 50% of the magnitudes of

[1]MRI/JMA, NCEP, Meteorological Service of Canada (MSC), ZAMG, the National Meteorological Center (NMC) of the China Meteorological Administration and the Chinese Academy of Meteorological Sciences (CAMS).

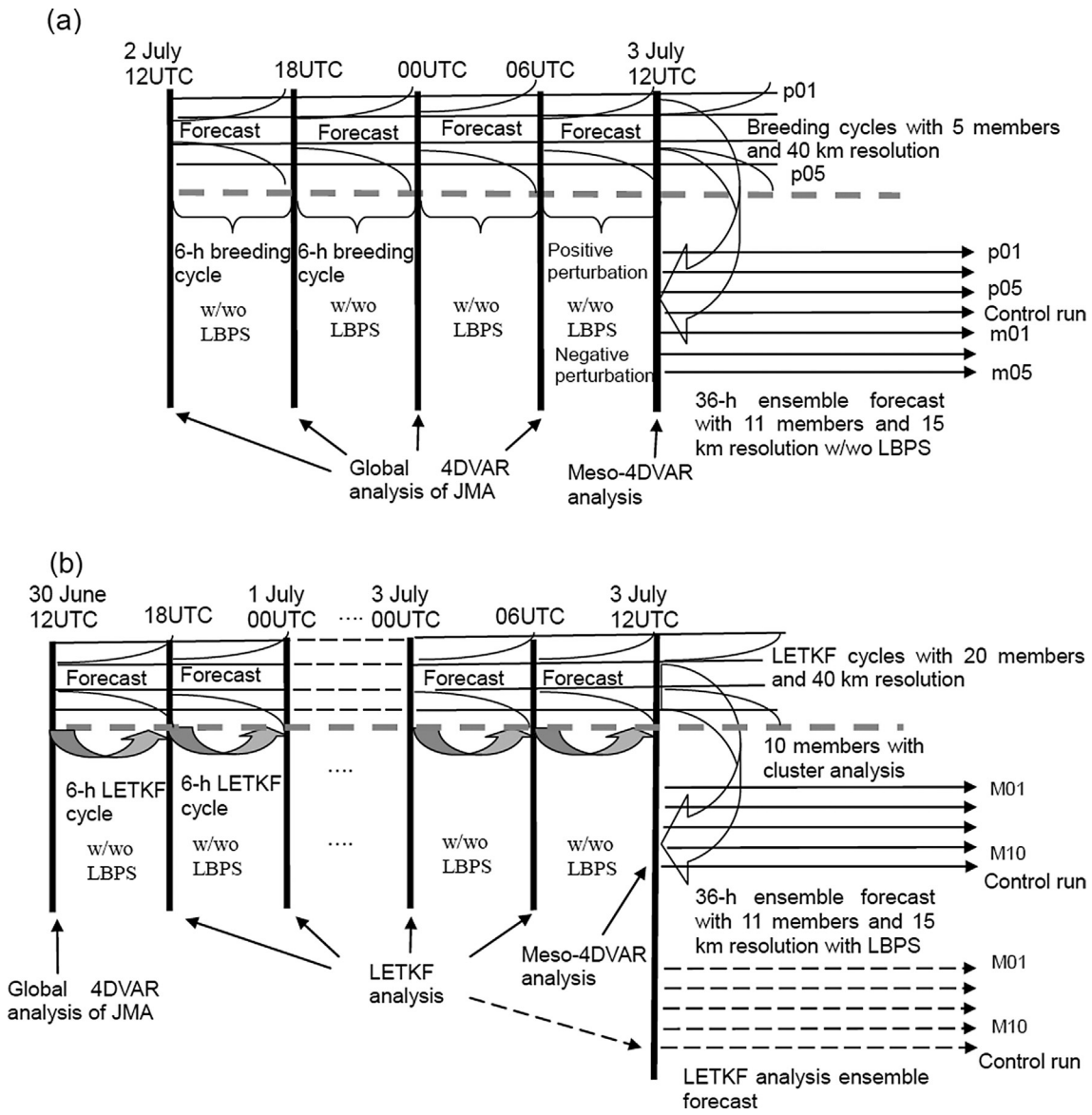

Fig. 1. Schematic diagrams of (a) the MBD method and (b) the LET method.

JMA's operational Meso 4D-VAR statistical background errors (Koizumi et al., 2005). To save computational time, forecasts in the breeding cycles were performed using the warm rain process.

Five independent breeding cycles were performed, and the five bred vectors were interpolated and added to the initial conditions of the control run to obtain five positive ensemble members at a horizontal resolution of 15 km. Additionally, the interpolated bred vectors were subtracted from the initial conditions of the control run to make five negative ensemble members. These negative members are essentially symmetric with respect to the positive members, but the ensemble mean is slightly modified owing to the super-saturation adjustment. S2011 describes more details about the breeding process such as the initial seed.

3.1.2. LETKF method We investigated the performance of NHM-LETKF (Miyoshi and Aranami, 2006) as the initial perturbations generator in the mesoscale EPS. The LETKF (Hunt et al., 2007) following the ETKF approach (Bishop et al., 2001) was used to solve the Kalman filter analysis equation for the covariance matrix. The analysis equation for LETKF is:

$$\mathbf{X}^a = \bar{x}^f e + \delta\mathbf{X}^f \left(\tilde{\mathbf{P}}^a (\mathbf{H}\delta\mathbf{X})^T \mathbf{R}^{-1} (y^o - \overline{H(x^f)}) e + \sqrt{m-1}\, \mathbf{U}\mathbf{D}^{-1/2}\mathbf{U}^T \right)$$
$$= \bar{x}^f e + \delta\mathbf{X}^f \tilde{\mathbf{P}}^a (\mathbf{H}\delta\mathbf{X})^T \mathbf{R}^{-1} (y^o - \overline{H(x^f)})\, e + \delta\mathbf{X}^f \mathbf{T}. \quad (2)$$

Here, x is the model variable, $\overline{x}^f$ the ensemble mean and $d\mathbf{X}$ the ensemble perturbation matrix. H is the observation operator and $\mathbf{H}$ is its tangent linear, y^o the observation, $\mathbf{R}$ the observation error covariance and e is an m-dimensional row vector (1, …, 1) where m is the ensemble size. $\tilde{\mathbf{P}}^a = \mathbf{U}\mathbf{D}^{-1}\mathbf{U}^T$ is the analysis error covariance matrix in the space spanned by forecast ensemble perturbations ('tilde space'), and $\mathbf{U}$ and $\mathbf{D}$ are obtained by an eigenvalue decomposition. The first term is the background, the second term is the analysis increment and the third term is the ensemble-perturbation update by the transform matrix **T.** In S2011, and in Sections 6.1 and 6.2 in this article, the third term was used as the ensemble perturbation generator and the first two terms were replaced by the Meso 4D-VAR analysis in the ensemble forecast. Note that rescaling in the breeding method corresponds to the use of a diagonal transform matrix, while $\mathbf{T}$ is non-diagonal in LETKF. Miyoshi (2010) gave the detailed formulation and its application to NHM. Hereafter, we call the initial perturbation method using LETKF as the 'LET method' or simply 'LET', according to S2011.

Figure 1b is an outline of the LET procedure and the ensemble prediction in B08RDP. As in the MBD method, 6-h EnKF forecast-analysis cycles with NHM (40 kmL40) were performed four times a day, but the ensemble size was increased to 20 to reduce the sampling errors in the analysis. A multiplicative inflation factor of 10% to the ensemble perturbations (i.e. 21% covariance inflation) was employed. Covariance localisation was performed with observation localisation scales of five horizontal grid points and three vertical levels, in which the influence of an observation is cut off when the distance is larger than the product of the localisation scale and 2.0*sqrt(10/3). Surface and upper sounding data including Aircraft Meteorological Data and Reporting data that passed the operational quality control (QC) procedures (Table 1) were assimilated by LETKF. The analysis ensemble was recentered around the analysis from the Meso 4D-Var system (Kunii et al., 2010) at every 12 UTC in the LETKF forecast-analysis cycles. Then, 10 members were selected by a cluster analysis based on distances evaluated by the variation of the normalised energy norm in the lower atmosphere (eq. (4) in S2011). To reduce the computation time, the warm rain process was adopted in the forecast-analysis cycles.

Miyoshi and Aranami's (2006) NHM-LETKF was modified by Seko (2010) as follows: (1) improved treatments of momentum (e.g. accurate treatment of air density) and pressure as prognostic variables, (2) implementation of vertical hybrid coordinates, (3) saturation adjustment of the initial field, (4) removal of local patches, (5) a cluster analysis procedure to choose 10 members from 20 members, and (6) introduction of LBPs in forecast-analysis cycles. Local patches, those originated from the local EnKF (Ott et al., 2004), were removed by the method of Miyoshi et al. (2007) to avoid a problem of analysis discontinuity. This method was implemented for NHM-LETKF by Fujita et al. (2009).

Table 1. List of data assimilated in the Meso 4D-VAR and LETKF analyses

	LETKF	Meso 4DVAR
GTS data	Radiosonde Pilot balloon Aircraft (AMDAR)	Radiosonde Pilot balloon Aircraft (AMDAR) Ship Buoy QuikSCAT sea surface winds
Domestic data	Non	Wind profiler in Japan Aircraft (domestic ACARS) Radar-AMeDAS analysed rainfall in Japan One-hour precipitation amount and total precipitable water retrieved from SSM/I, TMI and AMSR-E. Radial velocity data of operational Doppler radars in Japan

S2011 describes further details of the cluster analysis. Seko et al. (2011) performed mesoscale and cloud-resolving ensemble forecast experiments for a heavy rainfall event in western Japan using NHM-LETKF and obtained promising results.

3.2. *LBPs method*

The JMA operational one-week EPS was used for LBPs. Fig. 2 shows the procedure to prepare LBCs and LBPs. Perturbations were obtained from the JMA operational one-week EPS (TL319L60) by subtracting the control run forecast from the first five positive ensemble members. Although the horizontal resolution of the JMA one-week EPS is about 60 km, 6-h archived forecast grid point values (GPVs) with 12 pressure levels and horizontal resolution of 1.25° are used in B08RDP. These data cover the Regional Specialized Meteorological Center (RSMC) Tokyo responsible area (80–180°E, 0–71.5°N) and are transferred daily by the Numerical Prediction Division (NPD) of JMA in Tokyo to MRI in Tsukuba through an exclusive line. Because the highest level of the archived forecast GPV is at 100 hPa, which is lower than the top of the 40-level NHM (22.1 km; about 40 hPa), the forecast GPVs were first interpolated into the 6-h 32-level hybrid NHM (NHM L32) model levels (model top at 13.8 km; about 160 hPa),

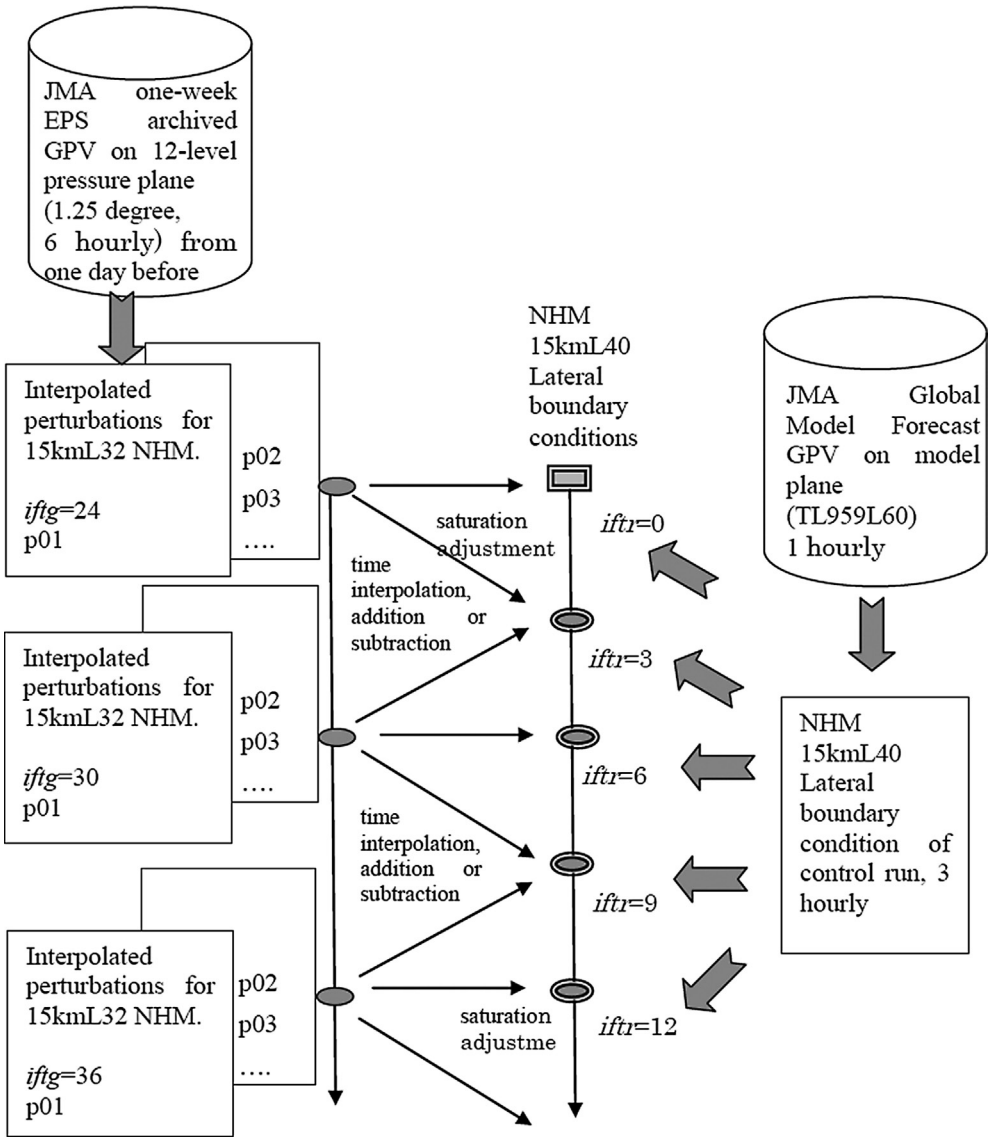

Fig. 2. Schematic diagram of the preparation procedure for LBCs and LBPs.

and the perturbations were obtained by subtracting the interpolated field of the control run from that of the perturbed runs. Then, the perturbations were normalised and added to the 3-h LBCs of the control run of the 40-level hybrid NHM (NHM L40). Perturbations at the NHM L32 32nd level were extrapolated to the top eight levels of NHM L40. At the *kz*-th level, the amplitudes of that perturbations were multiplied by the coefficient $c1 = \{1-\cos(\pi*(kz-40)/8)\}/2$, so that the perturbation amplitude would become zero at the top of NHM L40.

Because the data transfer timing of the RSMC Tokyo ensemble forecast GPVs from NPD/JMA to MRI was too late to conduct a near real-time EPS run of B08RDP, the RSMC data at 12 UTC of the day before were used. The amplitudes of the global EPS perturbations were adjusted to take into account the difference in initial times. To evaluate the forecast errors of JMA's operational global EPS, the statistical evolution of the ensemble spread of the 500 hPa height field (Figure 3) was adopted. The ensemble spread of the global EPS was defined by a function WEPSPR (FT), and the amplitude of perturbation at the global EPS FT = *iftg* (24–60 h) was adjusted by multiplying it by the following coefficient *c2*:

$$c2 = \frac{WEPSPR\,(iftr)}{WEPSPR\,(iftg)}, \tag{3}$$

where *iftr* is the FTof the mesoscale ensemble prediction (0–36 h). The value of *c2* is about 0.30 at the initial time of

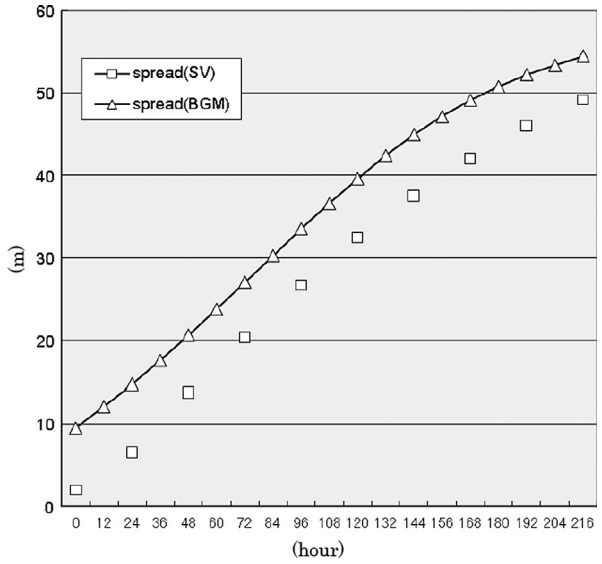

Fig. 3. Time sequence of the statistical ensemble spread of the 500 hPa height filed in the JMA's global one-week EPS. A line indicated by triangles is the spread by the global BGM before October 2007, whereas squares indicate the spread by the global SV method after November 2007. Courtesy of Ryouta Sakai of JMA.

the ensemble forecast ($iftr = 0$ and $iftg = 24$) and becomes 0.59 at the end of the 36-h ensemble forecast period ($iftr = 36$ and $iftg = 60$). After amplitude adjustment, perturbations were interpolated in time and space and added to the 3-h 40 km L40 LBCs for NHM produced by the JMA's high resolution global spectral model (GSM) forecast. The water vapour saturation adjustment was applied to all perturbed LBCs to avoid supersaturated conditions.[2]

Similar LBPs were prepared with a horizontal resolution of 40 km for breeding cycles in MBD and the EnKF data assimilation cycles in LETKF. For the initial time of the first breeding/EnKF cycles, $c2 = 1.00$ because $iftr = iftg = 0$, while $c2$ becomes 0.28 at the end of the fourth breeding/EnKF cycles ($iftr = 6$ and $iftg = 24$).

[2]A similar procedure was employed in the ensemble prediction of the Myanmar cyclone Nargis (Saito et al., 2010b), but in the case of the Nargis' EPS, the 6-h RSMC Tokyo responsible area data were not used because of their limited coverage. As an alternative, another 11-levels 12-h global EPS forecast dataset was used. Amplitudes adjustment with eq. (3) was not performed because the JMA one-week ensemble result at 12 UTC of the same day was available.

4. Design of the experiments

4.1. Breeding/EnKF cycles

In the breeding/EnKF cycles, the model domain (Figure 4) has 97×73 grid points with a horizontal resolution of 40 km. The number of vertical levels is 40, with the lowest level at 20 m above ground level, and the depth of the layers stretches from 40 to 1180 m with increasing height. Near lateral boundaries, absorbing layers of six grid points (240 km) are inserted with Rayleigh damping using a 1/e-folding time of 2400 s, whereas in the upper eight layers, levels 33–40, similar absorbing layers are employed to prevent false reflection of internal gravity waves.

In MBD, five-member 6-h breeding cycles were conducted successively from 12 UTC 2 July (Fig. 1a), with initial seeds given by perturbations from the operational global one-week EPS of JMA. Initial conditions of the control runs were prepared using JMA's operational global 4D-VAR analysis 6 hourly. In the LET method, 20-member 6-h EnKF cycles were conducted successively from 12 UTC 30 June (Fig. 1b), with the initial seeds prepared using high-resolution (0.1875°) global analyses of JMA at different analysis times. The observational dataset used in the operational global analyses of JMA after the QC procedures, except for satellite radiances, was assimilated by the LETKF.

LBCs of the control run were given by the JMA's operational high resolution GSM (TL959L60), whereas the LBPs described in Section 3.2 were added to the ensemble members. Physical processes were the same as in the ensemble forecast, but the warm rain process was used for the cloud microphysics to save computational time.

4.2. Ensemble forecasts

The ensemble forecasts at a horizontal resolution of 15 km were performed for 2 d, 3 and 4 July 2008, with initial times of 12 UTC up to a 36-h FT with 11 ensemble members. The model domain comprised 232×200 grid points, and vertical coordinates were the same as in the Breeding/EnKF cycles. Near lateral and upper boundaries, similar absorbing layers were also employed.

Initial conditions and LBCs of the control run were prepared by the Meso 4D-VAR analyses over the Beijing area (Kunii et al., 2010) and by JMA's high-resolution operational GSM forecast (Japan Meteorological Agency, 2007), respectively.

A three-ice bulk cloud microphysics scheme that predicts cloud water, rain, cloud ice, snow and graupel and a Kain–Fritsch convective parameterisation scheme are included as the moist processes. Other physical processes including the

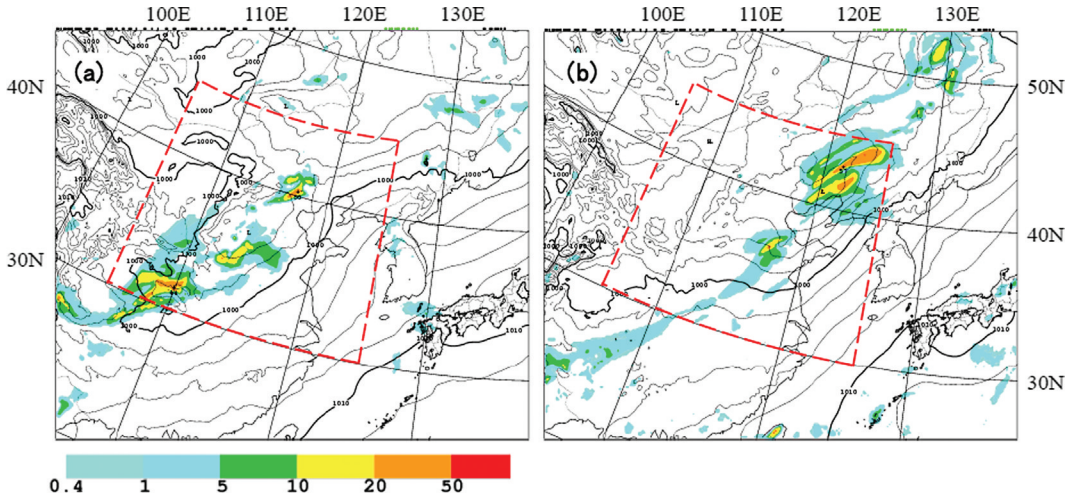

Fig. 4. Sea level pressure (contours) and accumulated 3-h precipitation (colour scale) predicted by the control run. Initial time is 12 UTC, 4 July 2008. The colour bar indicates precipitation intensity in mm. (a) FT = 3. (b) FT = 24.

atmospheric radiation were basically the same as in JMA's operational mesoscale model (MSM; Saito et al., 2006, 2007; Japan Meteorological Agency, 2007).

For more detailed specifications of the mesoscale EPS and modifications to the forecast model in B08RDP, see S2011.

4.3. *Comparison experiments*

To examine the effect of LBPs in the Breeding/EnKF cycles and 36-hr ensemble forecasts on EPS, we conducted six experiments using 4DVAR analysis data for initial conditions (Table 2). Additional two ensemble forecasts (LET_kfbf and LET_kfbfc) with control run initial conditions given by LETKF analyses are described in Section 7.4.

Table 2. List of experiments

Name	Initial condition of the control run	Initial perturbations	LBPs in breeding/ EnKF cycles to produce initial perturbations	LBPs in the ensemble forecast
NIP_lbpf	4DVAR	No	–	Yes
MBD_nlbp	4DVAR	BGM	No	No
MBD_lbpf	4DVAR	BGM	No	Yes
MBD_lbpfc	4DVAR	BGM	Yes	Yes
LET_lbpf	4DVAR	LETKF	No	Yes
LET_lbpfc	4DVAR	LETKF	Yes	Yes
LET_kfbf	LETKF	LETKF	No	Yes
LET_kfbfc	LETKF	LETKF	Yes	Yes

During the period of comparison, a synoptic low pressure system passed over eastern China. Fig. 4 shows the control forecast without perturbations at the initial time 12 UTC, 4 July 2008. A low pressure system was located southwest of Beijing at 15 UTC, 4 July (Fig. 4a; FT = 3) and moved northeastward bringing rainfall to the area northeast of Beijing on 5 July (Fig. 4b; FT = 24).

5. Effect of LBPs in MBD

5.1. *Pure effect of LBPs*

First, we see the ensemble characteristics purely due to the LBPs with no initial perturbations for reference ('NIP_lbpf' experiment). Figure 5 shows the ensemble spread horizontal distribution for meridional horizontal wind (V) at 850 hPa. Even without initial perturbations, if we apply the LBPs to the forecast, the ensemble spread soon increases near the lateral boundaries by FT = 3 (Figure 5a), and the influence of the LBPs propagates inside the model domain. By FT = 24, the spread has grown around the synoptic disturbance, and eventually a distinct large spread area appears corresponding to a low pressure system northeast of Beijing at FT = 36 (Fig. 5b).

Fig. 5c shows the evolution of the ensemble spreads of surface variables in the common verification area (105 ~ 125°E, 30 ~ 45°N; see Fig. 4). The ensemble spread gradually increases with time from zero at the initial time without the initial perturbations. The spread of mean sea level pressure (Psea) increases most rapidly because pressure difference propagates with the speed of sound waves. Spreads increase almost linearly during the 36-h forecast period and reach about 1 m/s for meridional wind (V), 0.8 hPa for surface pressure, 0.5°C for temperature (T) and

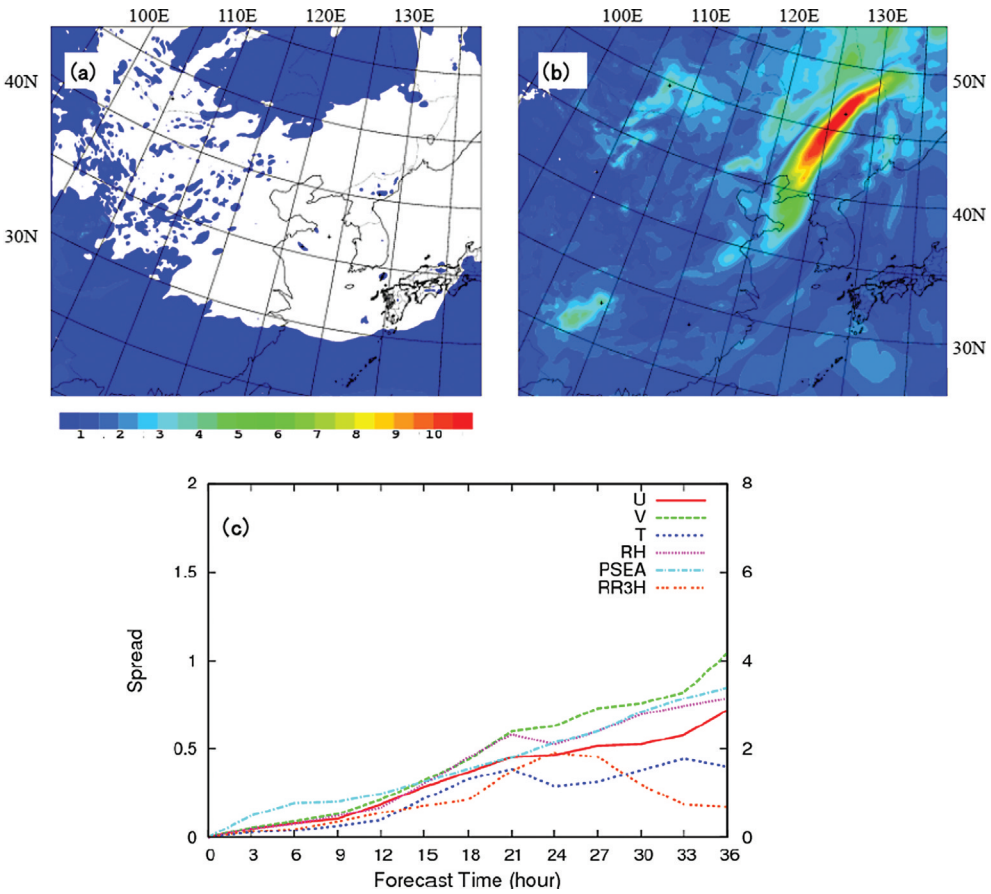

Fig. 5. (a) Ensemble spread for meridional horizontal wind (V) at 850 hPa in the experiment with LBP only (NIP_lbpf). Initial time is 12 UTC 4 July 2008. (b) Ensemble spread at FT = 36. (c) Time sequence of the ensemble spreads of surface elements in the common verification area.

3% for RH. The spread of 3-h accumulated rain (RR3H) decreases after FT = 27 owing to the passage of the low pressure system.

RMSEs of the control run at FT = 24 against the initial condition (analysis at 12 UTC 5 July) were almost the same for zonal wind (U), T and Psea but slightly smaller than those of the control run for V and RH (figures not shown, see Fig. E-5-4 of Saito et al. 2010a), which means that even with no initial perturbations, the mesoscale EPS with LBPs act as an ensemble forecast up to a point and may improve the accuracy of the ensemble mean.

5.2. *Ensemble forecast without LBPs*

Next, we confirm mesoscale EPS features without LBPs and investigate the characteristics of the bred vectors (the 'MBD_nlbp' experiment). Figure 6a, b shows the horizontal maps of the ensemble spread for V at 850 hPa at FT = 0 and FT = 36, respectively. In this case, the bred vectors cannot grow near the lateral boundaries; thus, the initial perturbations are confined to inside of the model domain (Fig. 6a). The ensemble spread remains small and even decreases slightly near the lateral boundaries in the forecast period. At FT = 36, the spread is small and has barely grown around the low pressure system (Fig. 6b).

Fig. 6c shows the evolution of the ensemble spread for surface variables. The spreads reach maximum values at around FT = 24 and then start decaying. The temperature ensemble spread increases in the day time (FT = 12–21), corresponding to the diurnal cycle.

Enlarged views of the horizontal distribution of surface precipitation at FT = 24 are shown in Fig. 9a. Here, only members 'p05' and 'm05' are shown in the left two columns. Precipitation patterns by each ensemble member are similar. The ensemble spread (the right most column) also had a pattern similar to that of the ensemble mean (the second right column), suggesting that the ensemble dispersion was mainly due to small positional differences of intense rainfalls.

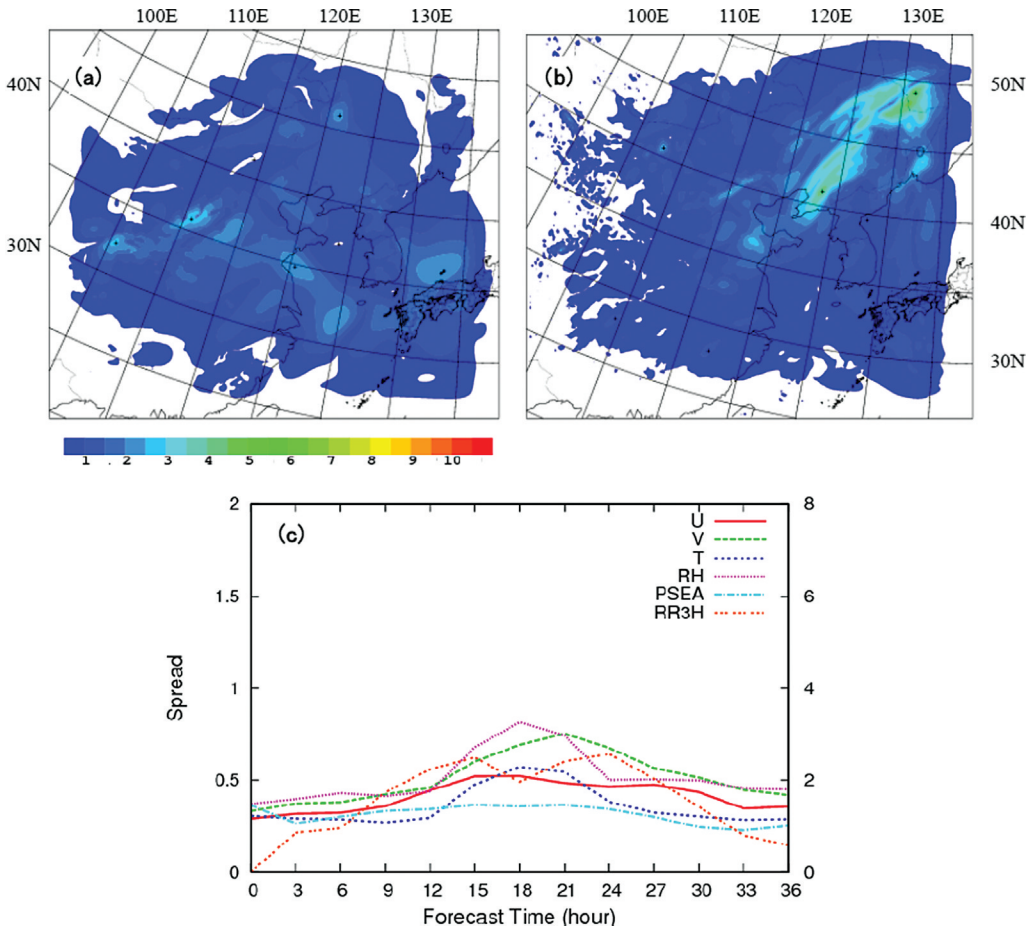

Fig. 6. Similar to Fig. 5 but for the MBD experiment without LBPs (MBD_nlbp).

5.3. *Effect of LBPs in the ensemble forecast*

In this experiment, LBPs described in Section 3.2 are interpolated and introduced in the 36-h ensemble forecast with a horizontal resolution of 15 km. When LBPs are introduced (the 'MBD_lbpf' experiment), ensemble spreads in the latter half of the period (after FT = 18) become larger. Fig. 7a, b shows the horizontal maps of ensemble spread for V at 850 hPa in the MBD experiment including LBPs. Although the ensemble spread at FT = 0 (Fig. 7a) is identical to that of MBD_nlbp (Fig. 6a), the ensemble spread at FT = 36 (Fig. 7b) extends throughout the model domain, and the amplitude of the spread around the low pressure system becomes larger compared to the results for MBD_nlbp (Fig. 6b). However, Fig. 7b is similar to Fig. 5b, suggesting that at FT = 36, the influence of LBPs is dominant and that bred initial perturbations may contribute only slightly to the spread. This implication is confirmed by the time series of the ensemble spread (Fig. 7c). Spreads for MBD_lbpf are larger than those for MBD_nlbp (Fig. 6c) in the second half of the forecast period, but at FT = 36, MBD_lbpf spreads are not far from those obtained in the experiment without initial perturbations (NIP_lbpf; Fig. 5c).

5.4. *Effect of LBPs in breeding cycles*

The above results suggest that ensemble spreads in MBD_lbpf were mainly contributed by LBPs in the latter half of the forecasts and that the initial MBD perturbations did not grow much. To further examine the effect of LBPs in breeding cycles, LBPs were applied not only to the ensemble forecast but also to the breeding cycles at a horizontal resolution of 40 km (the 'MBD_lbpfc' xperiment).

Figure 8a, b shows the horizontal distributions of the ensemble spread of V at 850 hPa. The bred initial perturbations at FT = 0 (Fig. 8a) are distributed over the whole forecast domain and their amplitudes have become larger. Compared with MBD_lbpf (Figure 7a), the location of the large initial spread area in central China has shifted southwestward, so that the positional correspondence with the low pressure system is improved. The differences

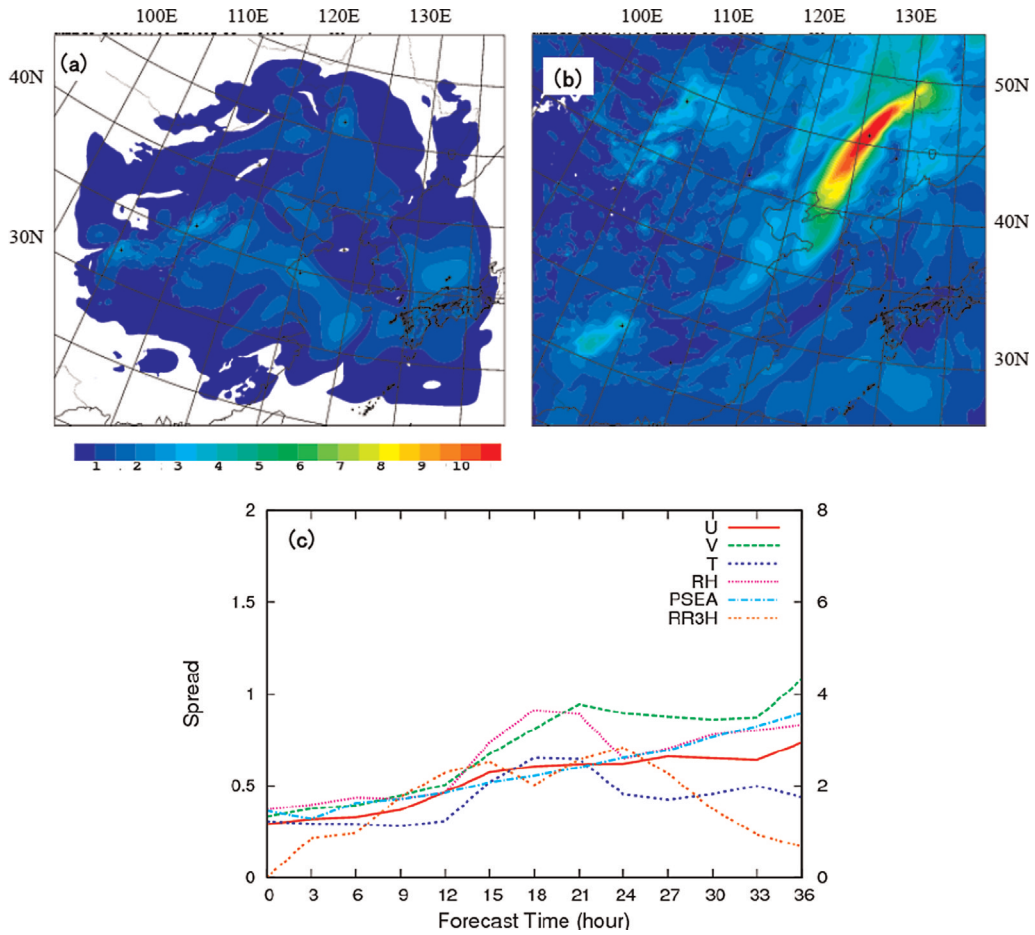

Fig. 7. Similar to Fig. 6 but with LBPs in the ensemble forecast (MBD_lbpf).

between MBD_lbpfc and MBD_lbpf continue throughout the ensemble forecast period. At FT = 36 (Fig. 8b), the spread is larger and more solid than in Figure 7b.

Time series of ensemble spreads is shown in Figure. 8c. The spreads become larger from the initial time and tend to increase throughout the forecast period. Diurnal changes in the spreads of surface temperature and relative humidity become more distinct. This suggests that each member has its own weather, and diurnal change in each member is different. The magnitudes of the ensemble spreads at FT = 36 are much larger than those of MBD_lbpf. Interestingly, even though the same LBPs were applied to MBD_lbpfc and MBD_lbpf in the ensemble forecast, the differences in spread amplitudes at FT = 36 between them (compare Fig. 8c and 7c) are larger than those between MBD_lbpf (Fig. 7c) and NIP_lbpf (Figure 5c). Namely, LBPs in breeding cycles play an important role in producing growing bred vectors that in turn increase the forecast ensemble spread more effectively than the LBPs in the ensemble forecast period.

Fig. 9b shows 3 h accumulated precipitation at 12UTC 5 July (FT = 24) by MBD_lbpfc. Member 'p05' predicts two separate rainfall bands, one east and one south of Beijing (double circle), whereas member 'm05' predicts an intense rainfall region northeast of Beijing. Large ensemble spread areas extend further southwest than in MBD_nlbp (Figure 9a).

The introduction of LBPs in the breeding cycles contributes not only to increasing the ensemble spread but also to improving the accuracy of the ensemble mean. Averaged RMSEs for two initial times (3 and 4 July 2008) for the control runs and for the MBD ensemble forecasts are shown in Fig. 10. Compared with the control run (single deterministic forecast), the ensemble mean RMSEs for surface variables are smaller even without LBPs (MBD_nlbp) (Fig. 10a). If we apply LBPs in the ensemble forecast (MBD_lbpf), RMSEs become smaller. The advantage of the ensemble forecast is the most distinct in MBD_lbpfc, where LBPs are introduced in the breeding cycles. The 500 hPa level verifications yield the same conclusion (Fig. 10b).

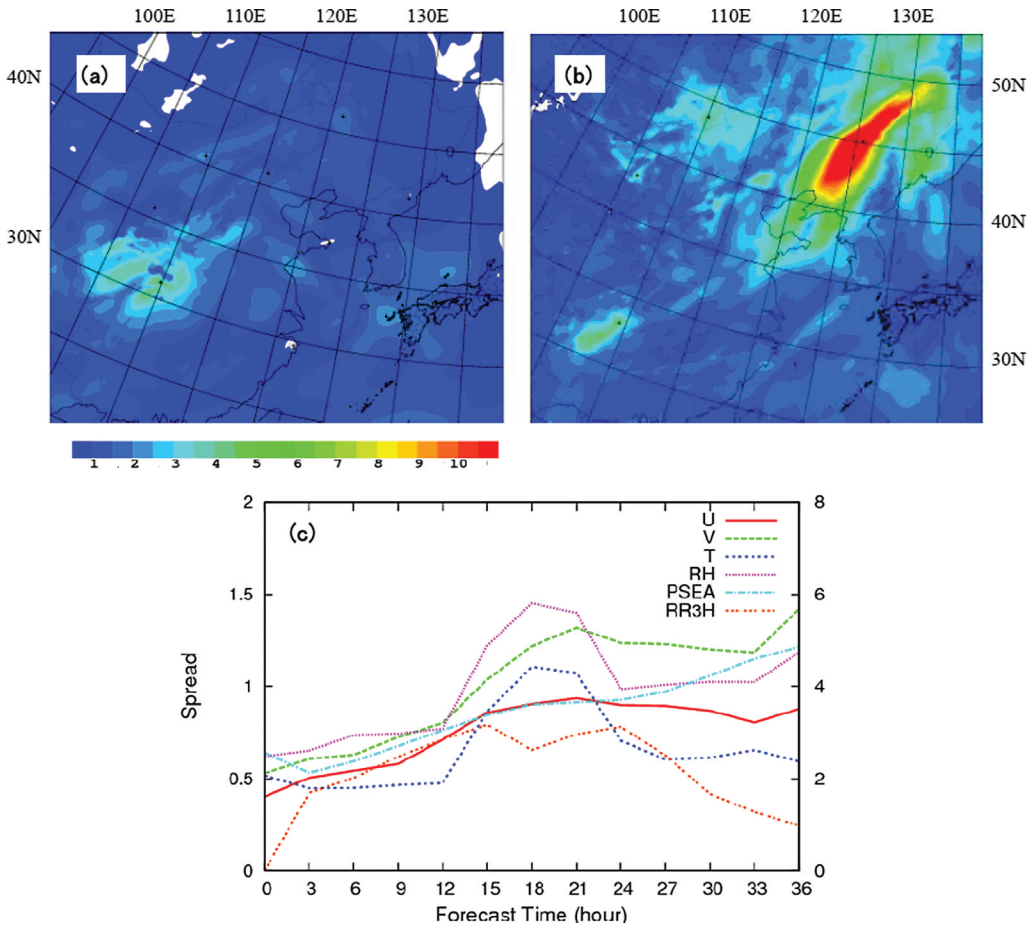

Fig. 8. Similar to Fig. 7 but with LBPs in both breeding cycles and the ensemble forecast (MBD_lbpfc).

6. Effect of LBPs in LETKF

Similar experiments as in the MBD method were performed with the LETKF ('LET' experiment). Because the advantage of LBPs in the ensemble forecast was obvious, as described in Section 5, we focus on the effect of LBPs in the LETKF cycles in this section. LBPs described in Section 3.2 are introduced in the 36-h ensemble forecast with a horizontal resolution of 15 km.

6.1. *Ensemble forecast with the LET method*

Fig. 11a, b shows the ensemble spread of V at 850 hPa by the LETKF when LBPs were introduced in the ensemble forecast ('LET_lbpf'). Because the LBPs were omitted in the EnKF forecast analysis cycles in this experiment, no initial spreads are seen near the lateral boundaries (Fig. 11a). At FT = 36, the large spread area has moved northward to a location, corresponding to that of the low pressure system (Fig. 11b). These distributions of the ensemble spread are similar to those obtained with MBD_lbpf (Fig. 7a, b) except that the amplitude of spread in LET_lbpf is slightly smaller than that in MBD_lbpf. Initial perturbations of LET are smaller than those in MBD over Japan and around Beijing, where the observation density is high. This suggests that the LET generates initial perturbations that represent the accuracy of the analysis.

Fig. 11c shows the evolution of the ensemble spreads of surface fields in the common verification area. The characteristics of the spreads are similar to the corresponding results in MBD_lbpf (Fig. 7c), but the diurnal cycles in temperature and relative humidity in the day time are somewhat smaller than those in the MBD method. Spreads at FT = 36 are almost the same as those in NIP_lbpf and MBD_lbpf (Fig. 5c and 7c, respectively), suggesting that the influence of LBPs is dominant.

The 3-h accumulated precipitation at 12UTC 5 July (FT = 24) resembled that in MBD_lbpf, and the results produced by each member were similar to the ensemble mean (figure not shown, see Fig. E-5-20 of Saito et al. 2010a).

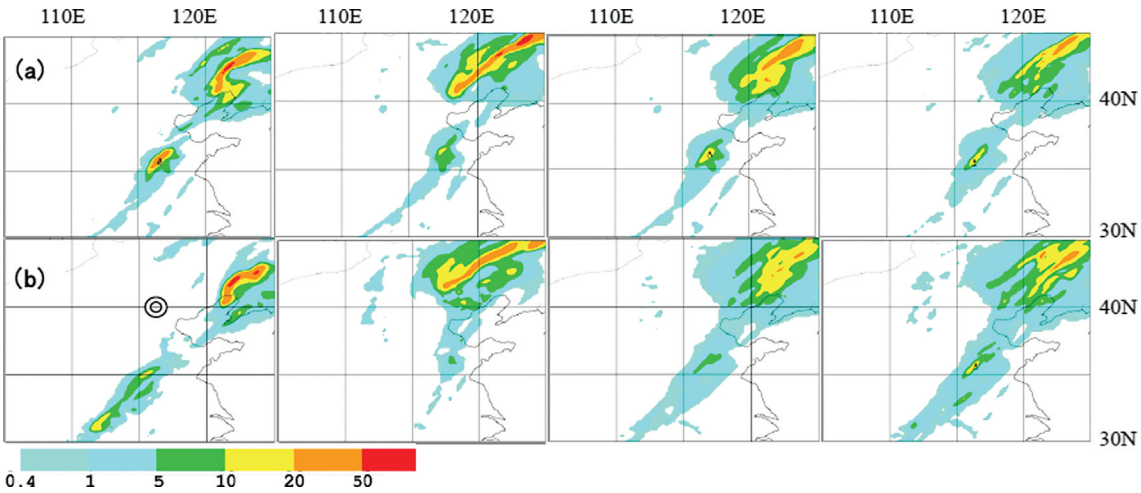

Fig. 9. Three-hour accumulated precipitation at 12UTC 5 July (FT = 24) predicted by each member. From left, member p05, member m05, the ensemble mean and the ensemble spread. (a) MBD method without LBPs (MBD_nlbp). (b) MBD method with LBPs in both breeding cycles and the ensemble forecast (MBD_lbpfc).

6.2. Effect of LBPs in EnKF cycles on ensemble prediction

In this experiment, LBPs were applied not only to the ensemble forecast but also to the EnKF forecast analysis cycles of LETKF with a horizontal resolution of 40 km ('LET_lbpfc'). The procedures described in Section 4.1 were applied to the 6-h EnKF cycles of LETKF from 12 UTC 30 June 2008.

Fig. 12a, b shows the ensemble spread horizontal distribution of V at 850 hPa. The analysed initial perturbations at FT = 0 (Fig. 12a) extend over the whole forecast domain and their amplitudes become larger compared with LET_lbpf. Compared with Fig. 11a, the location of the large initial spread area shifts southwestward, and the positional correspondence with the synoptic disturbance (the low pressure system) is improved. Note that the initial perturbations are still small over Japan and around Beijing, where the observation density is high. Unlike in MBD_lbpfc (Fig. 7b), in LET, the initial ensemble spread corresponds well to the observation density. The effect of initial perturbations continues throughout the forecast period of 36 h. At FT = 36, the spread (Fig. 12b) is larger and more solid than in LET_lbpf (Fig. 11b), although it is slightly smaller than that in MBD_lbpfc (Fig. 8b).

The evolution of the ensemble spreads is shown in Fig. 12c. Spreads become larger from the early stage of the forecast and continue increasing throughout the forecast period. The diurnal cycle becomes clearer than in Fig. 12c but slightly smaller than that of MBD_lbpfc (Fig. 8c), as discussed in S2011. Magnitudes of ensemble spreads at FT = 36 are also much larger than in Fig. 12c. The 3 h accumulated precipitation at 12UTC 5 July (FT = 24) shows that the individuality of each member is increased, similar to the MBD_lbpfc case (figure not shown, see Fig. E-5-23 of Saito et al. 2010a).

Averaged RMSEs for two initial times (3 and 4 July 2008) for surface and 500 hPa variables are shown in Fig. 13a, b. The ensemble mean RMSEs are smaller than those of the control runs, and the introduction of LBPs in EnKF cycles not only increases the ensemble spread but also improves the accuracy of the ensemble mean, which means that the RMSE/spread ratio approaches unity.[3] RMSEs of the ensemble mean decrease as a result of the implementation of LBPs in the forecast analysis cycle. RMSEs of LET_lbpfc were compared with those of MBD_lbpfc in Fig. 7 of S2011, where LETKF ensemble mean RMSEs were slightly larger than those for MBD.

7. Statistical evaluation and discussion

7.1. Evolution of energy norm

In the previous sections, we showed the evolution of ensemble spreads of the model surface variables in the ensemble predictions from MBD and LET perturbations for 12 UTC, 4 July 2008. The ensemble spread is a basic index that shows the properness of perturbations in EPS (Jolliffe and Stephenson, 2003), but its magnitude depends

[3]Comparison of RMSEs and ensemble spreads for MBD_lbpfc and LET_lbpfc has been given in Fig. 8 of S2011, where the ensemble predictions were still under dispersive compared with the model errors. Similar tendencies were seen in all mesoscale EPSs in the B08RDP intercomparison experiment (Kunii et al., 2011).

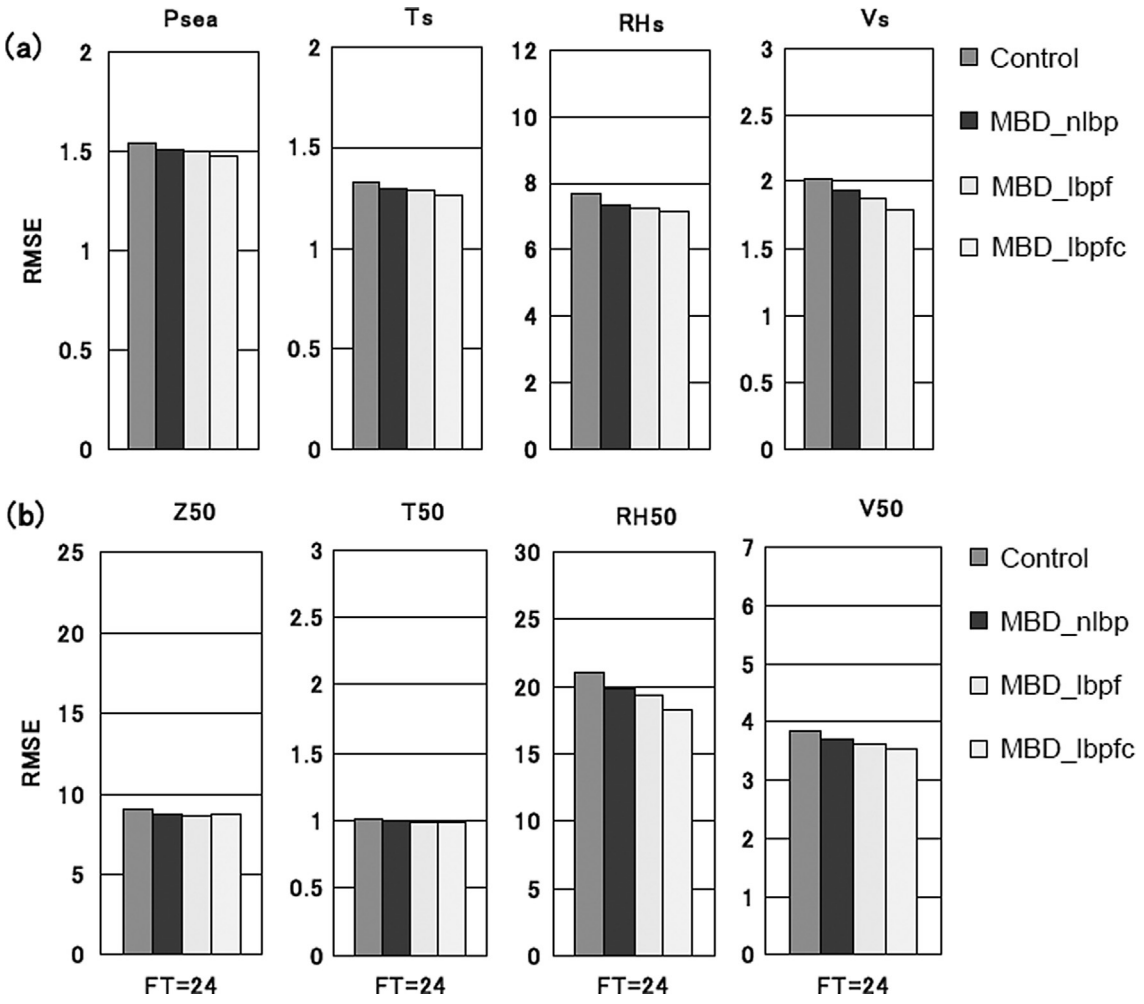

Fig. 10. (a) Averaged RMSEs against initial conditions for 3–4 July 2008 for surface variables. From left to right, Psea, T, RH and V. (b) Same as in (a) but for 500 hPa variables.

on how the perturbations are scaled. To investigate the initial ensemble variance and the growth of perturbations, magnitudes of the energy norms and their evolution in the ensemble prediction were examined. As in S2011, the TE norms by Barkmeijer et al. (2001) with wq = 0.2 in the common verification area were computed for the five vertical levels (surface, 850, 700, 500 and 250 hPa) and at 3-h intervals until FT = 24 for the two cases with initial times of 12 UTC, 3 July and 12 UTC, 4 July 2008.

Fig. 14a shows the evolution of the TE norms in the five ensemble experiments (MBD_nlbp, MBD_lbpf, MBD_lbpfc, LET_lbpf and LET_lbpfc) until FT = 24. All experiments showed steady growth of the TE norms, but the MBD_nlbp norm did not increase after FT = 18 owing to the fixed LBCs. The magnitude of the initial norms was the same in MBD_lbpf as in MBD_nlbp, but the MBD_lbpf norm increased throughout the simulation period. The TE norm of MBD_lbpfc was about twice that of MBD_lbpf at FT = 0, and it increased remarkably with time. Similar tendencies were seen in the LETKF norms. The TE norm of LET_lbpf was slightly larger than that of MBD_lbpf at the initial time, but it increased slightly more slowly compared with MBD_lbpf. The TE norm of LET_lbpfc was about twice that of LET_lbpf at FT = 0, and it increased with time, although the growth was somewhat more sluggish than that of LET_lbpfc, as discussed in S2011.

Figure 14b depicts the time series of the norm growth rates defined by the tendency of TE norms (slope of TE norm lines in Figure 14a). The growth rate of the MBD_nlbp norm was lowest among the three MBD methods, and after FT = 6, it became the lowest among all five experiments. When LBPs were introduced in the breeding (EnKF) cycles, the initial growth rate of MBD_lbpfc (LET_lbpfc) was larger than that of MBD_lbpf (LET_lbpf). After FT = 12, the growth rates of MBD_lbpf and LET_lbpf became seemingly larger than those of

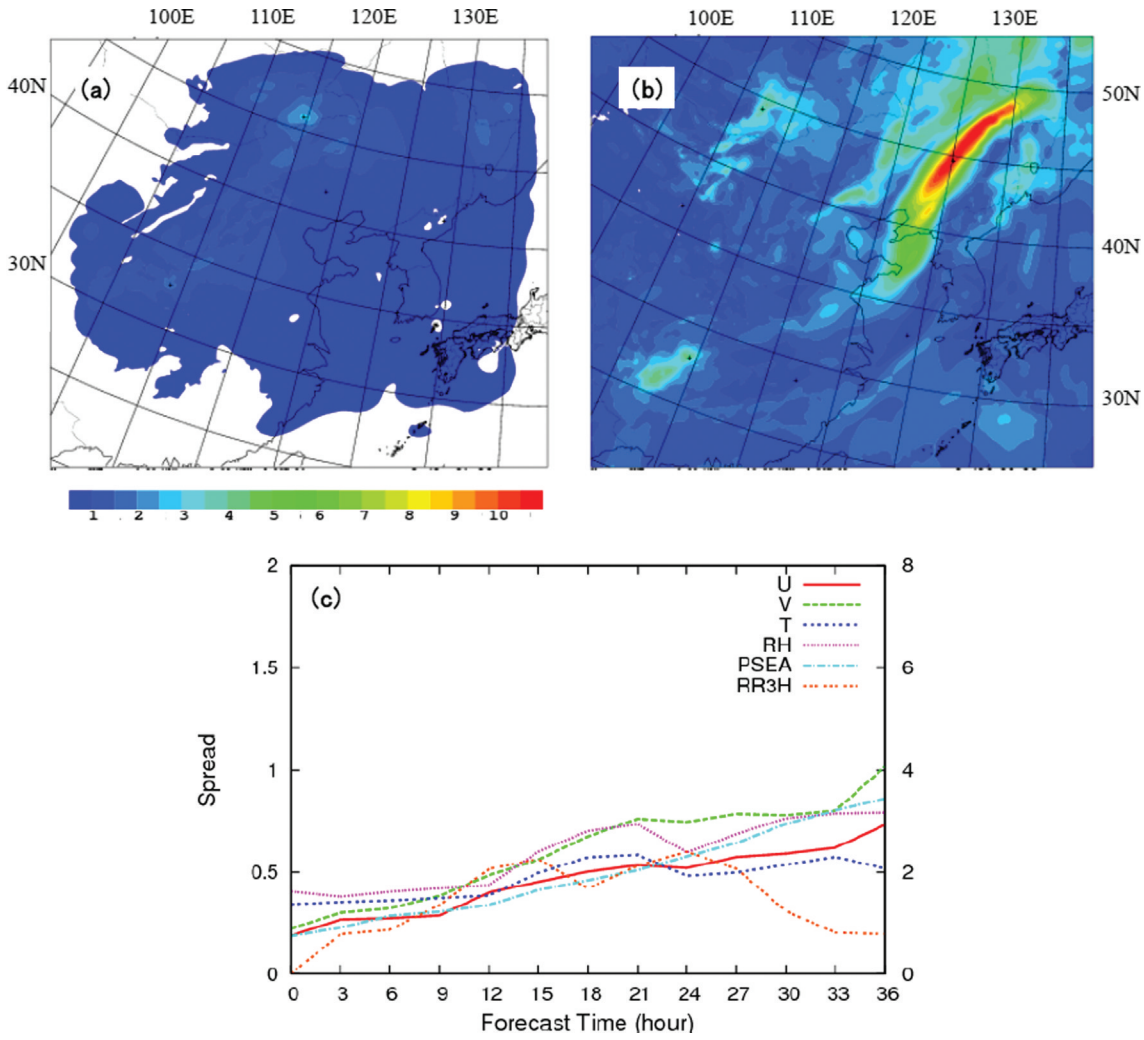

Fig. 11. Similar to Fig. 7 but for the LET method (LET_lbpf).

MBD_lbpfc and LET_lbpfc, respectively because the same LBPs were employed for all four experiments, and the absolute magnitudes of MBD_lbpfc and LET_lbpfc at the initial time were about twice as large as those of MBD_lbpf and LET_lbpf.

7.2. *Precipitation forecast performance*

We examined the precipitation forecast performances of the five ensemble experiments by computing BSSs that measure the skill of EPS as the probabilistic quantitative precipitation forecast. As in S2011, forecasted precipitations in the common domain were interpolated to verification grids with a resolution of 0.15° and compared with CMA's surface rain gauge network data (400 synoptic observation stations and 722 automated observation stations (Figure 1 of Kunii et al., 2011)).

Figure 15 shows the time series of BSSs for precipitation of 1 mm/6 h by the five experiments. Averages of two EPSs with initial times of 12 UTC, 3 July and 12 UTC, 4 July 2008, are depicted. Remarkable effects of the LBPs in the breeding/EnKF cycles are seen for all precipitation intensities. MBD_lbpfc showed the best performance among the five experiments, followed by LET_lbpfc. The better performance of MBD_lbpf compared to MBD_nlbp is not unexpected, but surprisingly, the performance difference between MBD_lbpfc and MBD_lbpf was much larger than that between MBD_lbpf and MBD_nlbp. This result means that the introduction of LBPs in the breeding cycles to produce bred vectors is more important than the introduction of LBPs in the ensemble forecast in the mesoscale BGM method.

Similar to the MBD method results, the difference in BSSs of LET_lbpfc and LET_lbpf was very large. Without LBPs

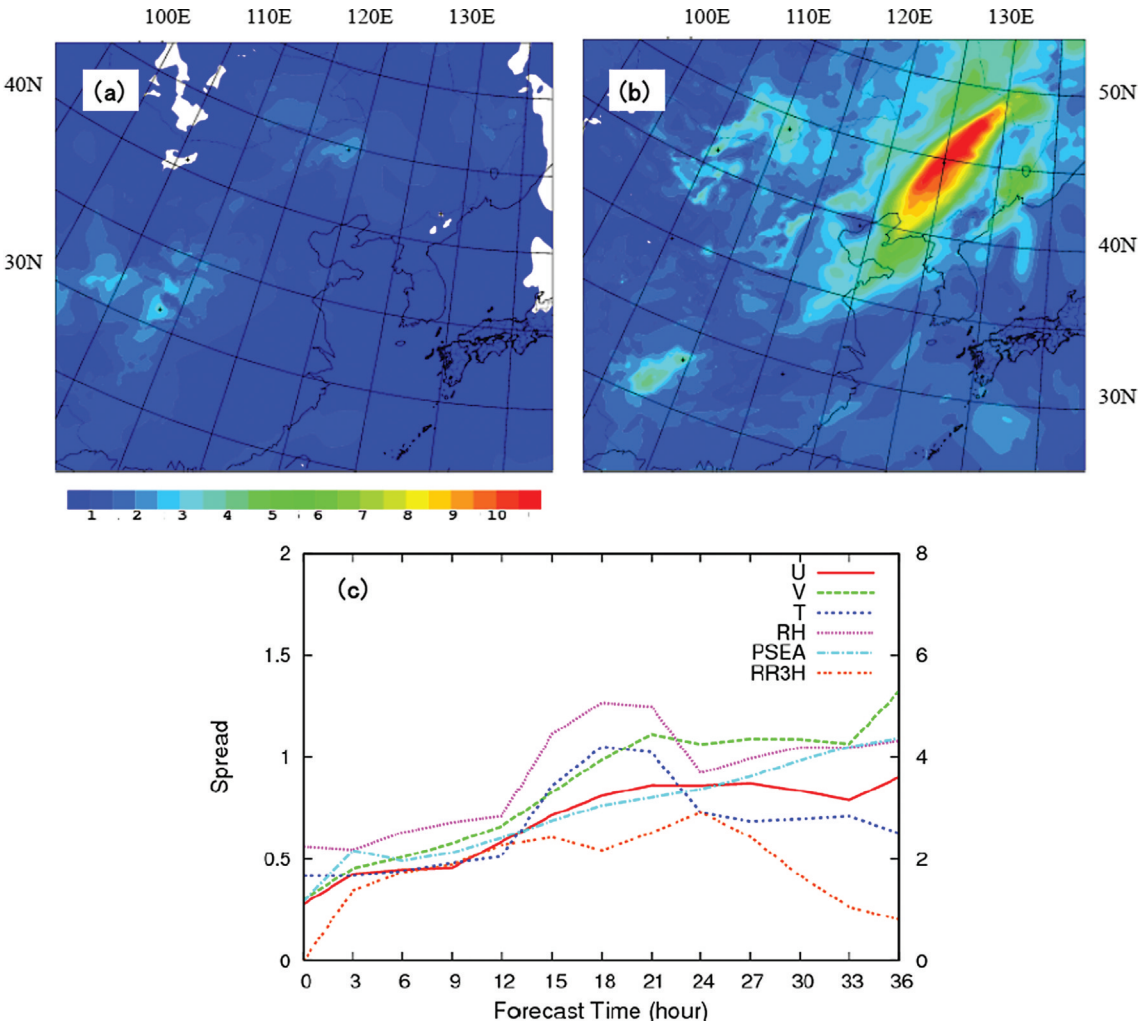

Fig. 12. Similar to Fig. 11 but with LBPs in both forecast analysis cycles and the ensemble forecast (LET_lbpfc).

in the EnKF cycles, LET_lbpf showed a poor performance for the precipitation forecast comparable to MBD_nlbp even with LBPs included in its ensemble forecast.

7.3. *Similarity index*

In the previous sections, the ensemble forecast performance was improved significantly by applying LBPs in the breeding/EnKF cycles. To examine the reason for the improvement, the orthogonality of initial perturbations was examined by computing the similarity index defined by:

$$SI = \left(\frac{\mathbf{a}}{\sqrt{(\mathbf{a},\mathbf{a})}}, \frac{b}{\sqrt{(\mathbf{b},\mathbf{b})}} \right). \tag{4}$$

Here **a** and **b** are bred vectors, (,) indicates the inner product and the norm operator is given by the moist TE norm eq. (1). The similarity index becomes 1 (–1) if the two vectors have the same (opposite) directions, and it becomes 0 if the two vectors are orthogonal. It is known that bred vectors tend to converge to the leading Lyapunov vector in the BGM method (Reynolds and Errico, 1999; Annan, 2004). Although this is not necessarily the case in operational global forecast models (Kalnay et al., 2002; Corazza et al., 2003), such a condition is not likely to be expected in the case of a limited area model under the strong forcing by LBCs.

Table 3a shows the similarity indexes between the bred vectors produced by the MBD method. Here, p1–p5 are positive perturbations and m1–m5 are negative perturbations. Because negative perturbations are obtained by subtracting the bred vectors, their directions are opposite to those of the positive perturbations with the same numbers except for a slight deformation due to the

Table 3. (a) Similarity indexes between bred vectors. Upper triangular matrix components indicate the case without LBPs in the breeding cycles (MBD_lbpf), and lower triangular matrix components show the case with LBPs in the breeding cycles (MBD_lbpfc). Values less than −0.4 or greater than 0.4 are indicated in boldface. (b) Same as (a) but for LET initial perturbations. Upper triangular matrix components indicate the case without LBPs in EnKF cycles (LET_lbpf), whereas lower triangular matrix components indicate the case with LBPs in EnKF cycles (LET_lbpfc)

	P1	p2	p3	P4	p5	m1	m2	m3	m4	m5
(a)										
p1	**1.00**	0.25	**0.50**	0.18	0.21	**−1.00**	−0.25	**−0.49**	−0.18	−0.21
p2	0.09	**1.00**	0.04	0.02	**0.62**	−0.25	**−0.99**	−0.03	−0.01	**−0.61**
p3	0.39	0.28	**1.00**	0.65	−0.05	**−0.49**	−0.03	**−0.99**	**−0.64**	0.06
p4	0.21	0.03	0.20	**1.00**	−0.18	−0.18	0.00	**−0.64**	**−0.98**	0.19
p5	−0.07	**0.53**	0.00	0.25	**1.00**	−0.20	**−0.61**	0.06	0.19	**−0.99**
m1	**−0.99**	−0.08	−0.37	−0.21	0.07	**1.00**	0.25	**0.50**	0.19	0.21
m2	−0.08	**−0.98**	−0.25	−0.02	**−0.52**	0.08	**1.00**	0.03	0.00	**0.62**
m3	−0.37	−0.26	**−0.97**	−0.19	0.01	0.37	0.27	**1.00**	**0.65**	−0.06
m4	−0.20	−0.02	−0.18	**−0.99**	−0.24	0.21	0.02	0.19	**1.00**	−0.19
m5	0.07	**−0.52**	0.02	−0.24	**−0.99**	−0.07	**0.53**	−0.01	0.24	**1.00**
	M1	M2	M3	M4	M5	M6	M7	M8	M9	M10
(b)										
M1	**1.00**	0.07	−0.23	−0.18	0.01	0.09	−0.03	**−0.46**	−0.30	−0.19
M2	−0.10	**1.00**	−0.11	−0.07	0.01	0.12	−0.31	−0.22	−0.33	−0.36
M3	0.19	−0.51	**1.00**	−0.06	**−0.40**	−0.34	−0.12	−0.03	0.27	0.03
M4	−0.18	−0.25	0.01	**1.00**	−0.22	−0.23	−0.02	−0.11	0.03	−0.15
M5	−0.10	0.32	−0.37	−0.26	**1.00**	0.06	−0.16	−0.01	−0.25	−0.02
M6	**−0.56**	0.12	−0.19	−0.02	0.06	**1.00**	−0.11	−0.07	−0.36	−0.18
M7	−0.01	−0.07	−0.07	−0.11	−0.17	−0.09	**1.00**	−0.14	0.10	−0.07
M8	0.03	−0.14	0.07	−0.10	−0.17	−0.17	−0.31	**1.00**	0.00	0.11
M9	−0.02	−0.27	0.09	−0.07	−0.15	−0.20	−0.20	−0.17	**1.00**	−0.02
M10	−0.23	−0.07	−0.26	−0.03	−0.14	0.07	0.00	−0.22	0.04	**1.00**

moisture saturation adjustment. Consequently, the similarity indexes between positive and negative perturbations with the same vector number are almost –1.0 (indicated with grey shade). In this table, upper triangular matrix components indicate the case without LBPs in the breeding cycles (MBD_lbpf), whereas lower triangular matrix components indicate the case with LBPs in breeding cycles (MBD_lbpfc). Values less than –0.4 or greater than 0.4 (indicated in boldface) mean that the angle between the two vectors is less than 66°. In MBD_lbpf, about 30% of bred vectors (12 of 40) were similar to each other. In MBD_lbpfc, the number of such similar vector pairs decreased drastically to 10% (4 of 40), indicating that the orthogonality of each vector was improved. The improvement of ensemble forecast performance (decrease in RMSEs and increase in BSSs) by LBPs in the breeding cycles is partly attributable to this effect.

Similarity indexes of initial perturbations were examined for the LET method as well. Table 3b shows the similarity indexes for the cases without and with LBPs in EnKF cycles. Unlike the MBD cases (Table 3a), orthogonalities between the initial perturbations were generally good even without LBPs in the EnKF cycles (LET_lbpf; upper triangle matrix components), and the similarity indexes were not very different from the case with LBPs (LET_lbpfc; lower triangle matrix components). In the case of LETKF, the bred vectors are linearly combined by the transform matrix, and the ensemble transform prevents the perturbation vectors from converging to a leading Lyapunov vector. In other words, orthogonality in the MBD method may depend on the characteristics of LBPs, whereas in LET, the independence of the transformed vectors does not rely on the orthogonality of LBPs. In the case of LET, LBPs in EnKF cycles are important not to underestimate the forecast errors and to keep the magnitude of the perturbation amplitude plausible.

7.4. Effect of LBPs in LETKF as the data assimilation scheme

In the previous sections, perturbations produced by the ensemble transform in LETKF were used only as initial

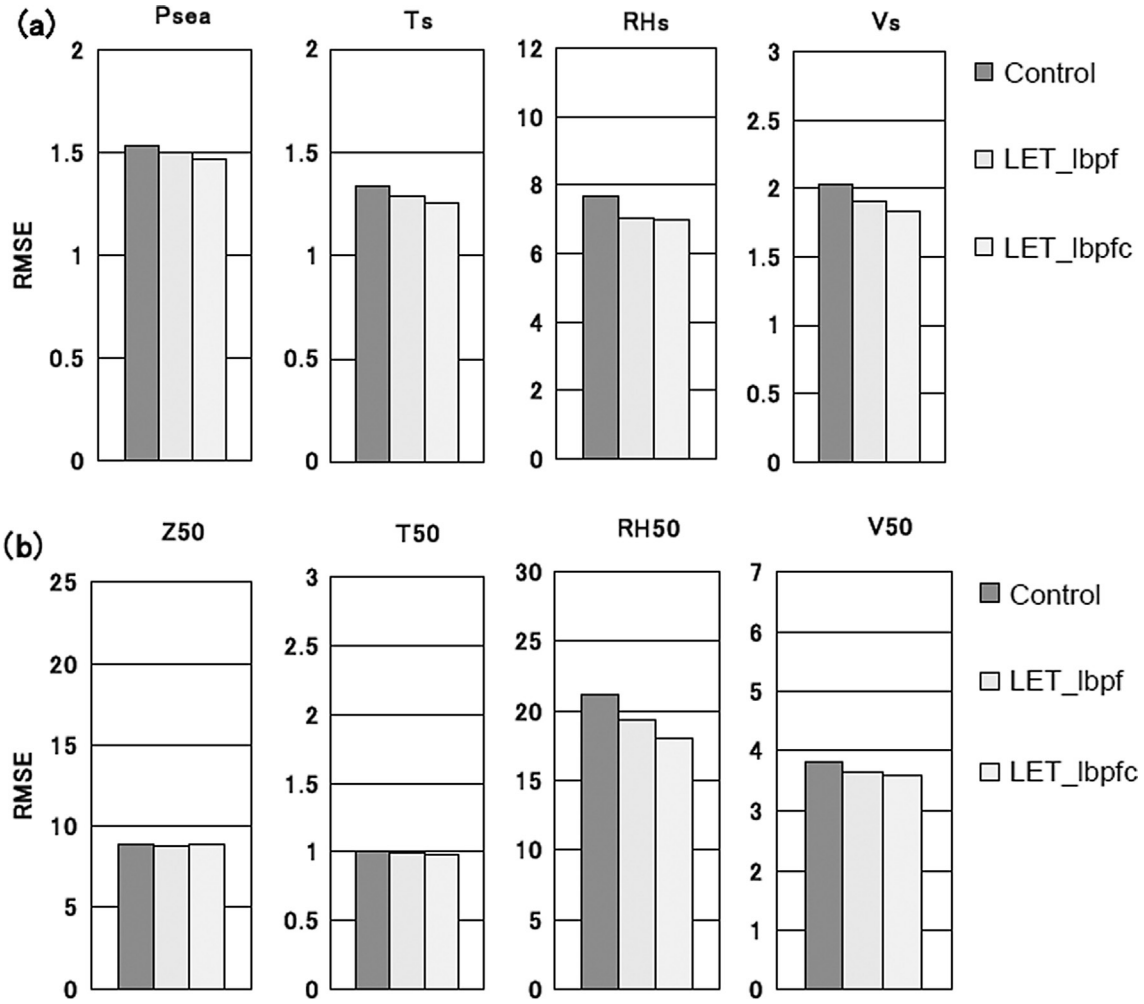

Fig. 13. Similar to Fig. 10 but for the LET method.

perturbations for a high resolution (15 km) ensemble forecast, and the initial conditions for the control run were replaced by the Meso 4DVAR analysis (Kunii et al., 2010). LETKF could produce its own analysis, but the analysis increment was discarded in the ensemble forecast initial condition. In the case of LETKF, the forecast error covariance is constructed by the ensemble perturbations; thus, without LBPs, forecast errors near lateral boundaries are underestimated. This underestimation of forecast errors results in underestimation of the Kalman gain near the lateral boundaries and would degrade the accuracy of the LETKF analysis. To investigate the differences in analysis accuracy, we conducted additional experiments in which the LETKF ensemble mean analyses were used as initial conditions for the control runs in the ensemble. Two experiments without and with LBPs in forecast-analysis cycles in LETKF were conducted (LET_kfbf and LET_kfbfc, respectively). LBPs in the ensemble forecast were used for both experiments.

With regard to the evolution of the ensemble spread, similar tendencies were seen as in the case of the Meso 4DAVAR analysis (LET_lbpfc and LET_lbpf), that is, ensemble spread grew more rapidly and diurnal cycles in surface temperature and relative humidity became more distinct if LBPs were present in the EnKF cycles (figures not shown, see Fig. E-5-26 of Saito et al. 2010a).

Figure 16 shows the forecast of LET_lbpfc. Despite the limitation of assimilated observation data (see Table 2), forecast fields from the LETKF analysis with LBPs in EnKF cycles are seemingly not inferior to those from the Meso 4DVAR analysis (Fig. 4).

Figure 17 compares RMSEs of 24-h forecasts from 12 UTC 4 July 2008 for the control run and the ensemble means from the LETKF analyses against the initial conditions (Meso 4DVAR analysis) of the day after. Here, the performance of LETKF as the data assimilation scheme is evaluated by examining the RMSEs of the control runs by LET_kfbf and LET_kfbfc along with those

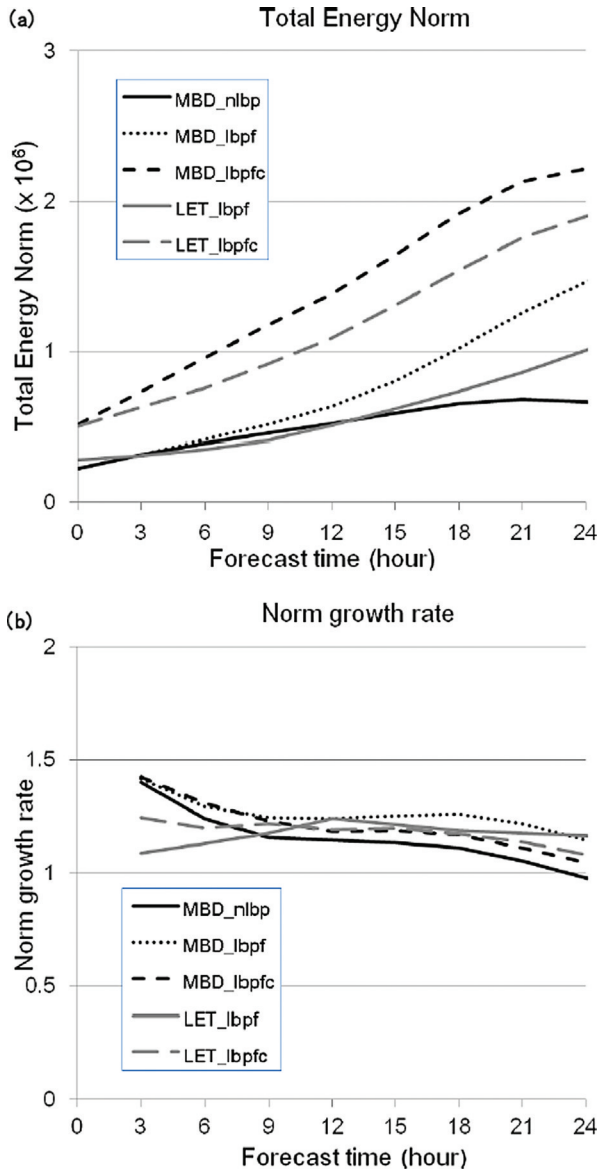

Fig. 14. (a) Time series of the TE norm. Averages of two EPSs with initial times of 12 UTC, 3 July and 12 UTC, 4 July 2008. (b) Time series of growth rate of TE norm.

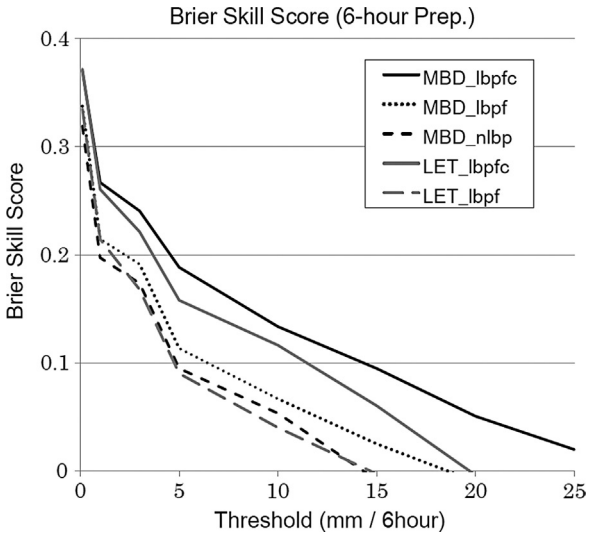

Fig. 15. Brier Skill Scores against different 6-h precipitation intensity thresholds for the five initial perturbation methods over two 36-h EPSs with initial times of 12 UTC, 3 July, and 12 UTC, 4 July 2008.

for the ensemble means. At the surface, RMSEs of the control run from LETKF analyses (LET_kfbf and LET_kfbfc) are larger than those of Meso 4D-VAR, except for V (Fig. 16a). When LBPs were introduced in the EnKF forecast-analysis cycles (LET_kfbfc), RMSEs of the control run decreased for RH but increased for Psea and Ts. At 500 hPa, RMSEs of the control run for LET were larger than those for Meso 4DVAR for T but smaller for Z500, RH and V. When LBPs were introduced in EnKF cycles, RMSEs of LETKF control run further decreased for all variables. These results indicate that the accuracy of the LETKF analysis improves with the presence of LBPs in the EnKF analysis cycles. RMSEs of the ensemble means (LET_kfbf_em and LET_kfbfc_em) were smaller than those of the control runs for all variables at both the surface and 500 hPa. Considering that in our study the number of LETKF ensemble members was limited (20) and RMSEs were evaluated against the initial conditions given by Meso 4D-VAR, this result seems promising in the sense that the LETKF analysis showed nearly comparable performance in RMSEs with the Meso 4D-VAR analysis for some variables.

8. Summary and concluding remarks

The effect of LBPs in mesoscale ensemble prediction using the mesoscale BGM method and the LETKF method was examined as a second part of MRI studies for WWRP B08RDP. An LBP method using the JMA's operational one-week global EPS was developed and applied to MRI's EPS for B08RDP. The amplitudes of LBPs were adjusted considering the global EPS's FTat the initial times of the mesoscale EPS and the associated breeding/EnKF cycles.

The influence of LBPs became dominant in the latter half of the 36-h ensemble forecast period, and even without initial perturbations the ensemble spread grew at local areas of uncertainty corresponding to mesoscale disturbances with the introduction of LBPs.

Three experiments (MBD_nlbp, MBD_lbpf and MBD_lbpfc) were conducted with the MBD method to examine the effect of LBPs in the ensemble forecast and

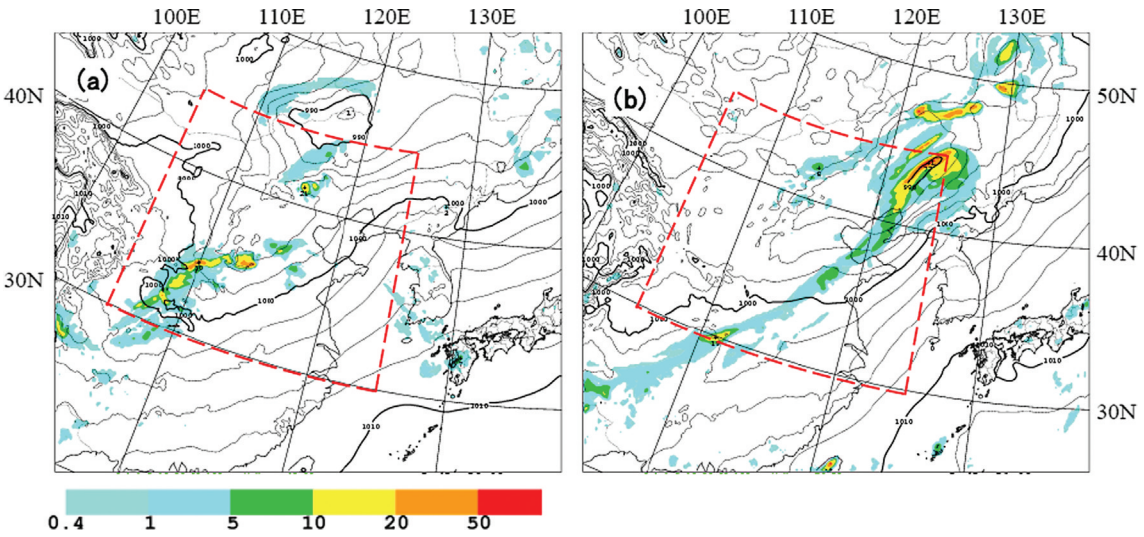

Fig. 16. Similar to Fig. 4 but by the control run with LETKF analysis (LET_kfbfc).

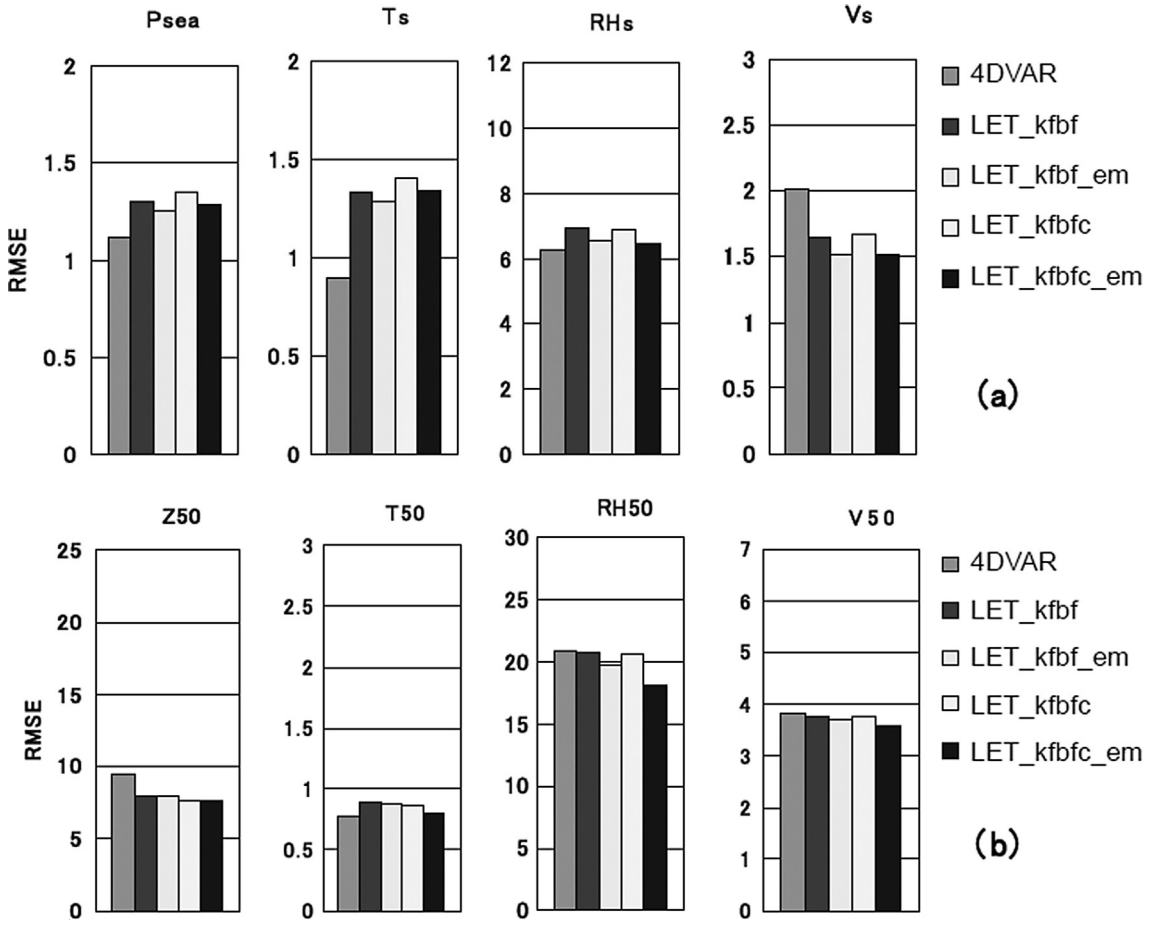

Fig. 17. (a) RMSEs of FT = 24 forecast fields from 4 July 2008 against the Meso 4D-VAR analysis of 5 July 2008 for surface variables. 4DVAR is the forecast from the 4DVAR analysis, whereas LET_kfbf and LET_kfbfc are forecasts from the LETKF analyses without and with LBPs in EnKF cycles, respectively. LET_kfbf_em and LET_kfbfc_em are their ensemble mean without and with LBPs in EnKF cycles. (b) Same as (a) but for 500 hPa variables.

the breeding cycles. In the MBD method, LBPs increased the ensemble spread and improved the accuracy of the ensemble mean in the 36-h ensemble forecast. When LBPs were introduced in the 6-h breeding cycles to produce the initial perturbations, the ensemble spread and RMSE of the ensemble mean were further improved in the ensemble forecast, and the effect lasted throughout the 36-h forecast period. Positional lags between the bred vectors and the locations of synoptic disturbances decreased with the introduction of LBPs in breeding cycles.

Two experiments (LET_lbpf and LET_lbpfc) were conducted with the LET method to examine the effect of LBPs in the EnKF data assimilation cycles. A similar tendency was seen with LET as with MBD. When LBPs were introduced in the 6-h EnKF cycles to produce the initial perturbations, the ensemble spread and RMSE of the ensemble mean were further improved in the ensemble forecast, and the effect continued throughout the whole period of the forecast. In the case of LETKF, LBPs in EnKF cycles also helped to prevent underestimation of the forecast error near the lateral boundaries.

Evolution of the TE norm was also examined. Inclusion of LBPs in the breeding/EnKF cycles doubled the amplitudes of initial perturbations and increased initial growth rates of the bred vectors and ETKF initial perturbations. Growth of perturbations for MBD was slightly larger than that for LET, as discussed in S2011. BSSs were computed to examine the performance of the quantitative probabilistic precipitation forecast by the mesoscale EPSs. MBD_lbpfc showed the best performance among the five experiments, followed by LET_lbpfc. Surprisingly, the performance difference between MBD_lbpfc and MBD_lbpf was larger than that between MBD_lbpf and MBD_nlbp, which means that the introduction of LBPs in the breeding cycles is more important than the introduction of LBPs in the ensemble forecast in the mesoscale BGM method. Similarly, without LBPs in the EnKF cycles, the precipitation forecast of LET_ lbpf was poor even if it included LBPs in its ensemble forecast.

We discussed the characteristics of the bred perturbation vectors by a similarity index analysis. In MBD_lbpf, about 30% of bred vectors were similar to each other, but the number of such similar vector pairs decreased to 10% if LBPs were introduced in the breeding cycles (MBD_lbpfc). In the case of the LET method, orthogonalities between the initial perturbations were generally good even without LBPs in the EnKF cycles owing to the ensemble transform.

The accuracy of the LETKF analysis was evaluated by comparing the RMSEs of the control run forecasts from the mesoscale 4D-VAR analyses. The accuracy of the LETKF analysis was also improved by the introduction of LBPs in the EnKF cycles. Despite the limitations of the experimental design for the LETKF, i.e. the small ensemble size (20) and unfavourable verification measure, some RMSEs of the forecasts from LETKF analyses showed values comparable to those from the Meso 4D-VAR analyses.

Our results show that the LBPs in mesoscale ensemble prediction are very important not only to enlarge the ensemble spread in the ensemble forecast but also to produce better initial perturbations and to improve the LETKF analysis when the LBPs are used in the breeding/EnKF cycles.

In this study (and in S2011), the relative advantage of the LET method as the initial perturbations generator against the MBD method was not necessarily clear. In S2011, we showed that with a small computational overhead, the MBD method yielded satisfactory results as an ensemble perturbation generator, especially for moderate to intense rains. There are several points in the LET method that should be further investigated such as the sensitivity to the choices of the ensemble size, inflation factor and localisation parameters. Recently, Miyoshi and Kunii (2011) developed the LETKF system with the WRF model and assimilateronymsd real observations. Their results showed that adaptive covariance inflation improved the forecast performance significantly. Orthogonality of LETKF perturbations did not depend on the LBPs, which may be an advantage of LET compared with MBD. The physical process perturbation should be implemented in non-linear models in MBD and LET to consider the model uncertainty. These topics are subjects for future studies.

9. Acknowledgements

The authors thank Dr. Tadashi Fujita of NPD/JMA for his courtesy in allowing us to use the modified version of NHM-LETKF. Thanks are extended to Masahiro Hara and Munehiko Yamaguchi of MRI and Tabito Hara of NPD/JMA for their help and support in conducting this study. We also thank Dr. Gong Jiandong and Dr. Duan Yihong of CMA for their efforts in organising B08RDP. This study was partly supported by the Japanese Ministry of Education, Culture, Sports, Science and Technology (MEXT) through a Grant-in-Aid for Scientific Research (21244074) 'Study of advanced data assimilation and cloud resolving ensemble technique for prediction of local heavy rainfall'.

Appendix

List of acronyms

ARPA-SMR	Agenzia Regionale Prevenzione e Ambiennte Romagna-Servizio Meteo Regionale
BGM	Breeding of Growing Modes
BSS	Brier Skill Score
B08FDP	Beijing 2008 Olympics Forecast Demonstration Project
B08RDP	Beijing 2008 Olympics Research and Development Project
CAMS	Chinese Academy of Meteorological Sciences
CMA	China Meteorological Administration
COSMO-LEPS	COnsortium for Small-scale MOdeling-Limited area Ensemble Prediction System
EnKF	Ensemble Kalman Filter
EPS	Ensemble Prediction System
ETKF	Ensemble Transform Kalman Filter
FT	Forecast Time
GPV	Grid Point Value
GSM	Global Spectral Model
GSV	Global model Singular Vector
JMA	Japan Meteorological Agency
LAEF	Limited Area Ensemble Forecasting
LET	Local Ensemble Transform (method)
LETKF	Local Ensemble Transform Kalman Filter
MBD	Mesoscale BreeDing growing mode (method)
MOGREPS	Met Office Global and Regional Ensemble Prediction System
MRI	Meteorological Research Institute
MSC	Meteorological Service of Canada
MSM	MesoScale Model
NCEP	National Centers for Environmental Prediction
NHM	Non-Hydrostatic Model
NMC	National Meteorological Center
NPD	Numerical Prediction Division
NWP	Numerical Weather Prediction
RSMC	Regional Specialized Meteorological Center
RMSE	Root Mean Square Error
SREF	Short-Range Ensemble Forecast
SV	Singular Vector
TE	Total Energy
WMO	World Meteorological Organization
WWRP	World Weather Research Programme
ZAMG	Zentralanstalt für Meteorologie und Geodynamik

References

Annan, J. D. 2004. On the orthogonality of bred vectors. *Mon. Wea. Rev.* **132**, 843–949.

Anthes, R. A., Kuo, Y.-H., Baumhefner, D. P., Errico, R. M. and Betgge, T. W. 1985. Predictability of mesoscale atmospheric motions. *Adv. Geophys.* **28**, 159–202.

Anthes, R. A., Kuo, Y.-H., Hsie, E.-Y., Low-Nam, S. and Bettge, T. W. 1989. Estimation of skill and uncertainty in regional numerical models. *Q. J. Roy. Meteor. Soc.* **115**, 763–806.

Barkmeijer, J., Buizza, R., Palmer, T. N., Puri, K. and Mahfouf, J. 2001. Tropical singular vectors computed with linearized diabatic physics. *Q. J. Roy. Meteorol. Soc.* **127**, 658–708.

Bishop, C. H., Etherton, B. J. and Majumdar, S. J. 2001. Adaptive sampling with ensemble transform Kalman filter. Part I: theoretical aspects. *Mon. Wea. Rev.* **129**, 420–436.

Bowler, N. E. 2006. Comparison of error breeding, singular vectors, random perturbations and ensemble Kalman filter perturbation strategies on a simple model. *Tellus* **58A**, 538–548.

Bowler, N. E., Arribas, A., Mylne, K. R., Robertson, K. B. and Beare, S. E. 2008. The MOGREPS short-range ensemble prediction system. *Q. J. Roy. Meteorol. Soc.* **134**, 703–722.

Bowler, N. E. and Mylne, K. R. 2009. Ensemble transform Kalman filter perturbations for a regional ensemble prediction system. *Q. J. Roy. Meteorol. Soc.* **135**, 757–766.

Corazza, M., Kalnay, E., Patil, D. J., Yang, S.-C., Morss, R. and co-authors. 2003. Use of the breeding technique to estimate the structure of the analysis 'errors of the day'. *Nonlin. Proc. Geophys.* **10**, 233–243.

Du, J., DiMego, G., Tracton, M. S. and Zhou, B. 2003. NCEP short-range ensemble forecasting (SREF) system: multi-IC, multi-model and multi-physics approach. *CAS/JSC WGNE* Res. *Act. Atmos. Ocea. Modell.* **33**, 5.09–5.10.

Duan, Y., Gong, J., Du, J., Charron, M., Chen, J. and co-authors. 2012. An overview of Beijing 2008 Olympics Research and Development Project (B08RDP). *Bull. Am. Meteor. Soc.* doi: 10.1175/BAMS-D-11-00115.1.

Errico, R. M. and Baumhefner, D. 1987. Predictability experiments using a high-resolution limited-area model. *Mon. Wea. Rev.* **115**, 488–504.

Fujita, T., Tsuguti, H., Miyoshi, T., Seko, H. and Saito, K. 2009. Development of a mesoscale ensemble data assimilation system at JMA. *Report of the Grant-in-Aid for Scientific Research (B)*(2005–2008), No. 17110035, 232–235 (in Japanese).

Hamill, T. M. and Colucci, S. J. 1997. Verification of Eta-RSM short-range ensemble forecasts. *Mon. Wea. Rev.* **125**, 1312–1327.

Hou, D., Kalnay, E. and Drogemeier, K. K. 2001. Objective verification of the SAMEX '98 ensemble forecasts. *Mon. Wea. Rev.* **129**, 73–91.

Houtekamer, P. L., Charron, M., Mitchell, H. L. and Pellerin, G. 2007. Status of the global EPS at Environment Canada. *Proc. ECMWF Workshop on Ensemble Prediction*, 57–68.

Hunt, B. R., Kostelich, E. J. and Szunyogh, I. 2007. Efficient data assimilation for spatiotemporal chaos: a local ensemble transform Kalman filter. *Physica D* **230**, 112–126.

Japan Meteorological Agency. 2007. Outline of the operational numerical weather prediction at the Japan Meteorological Agency. *Appendix to WMO Numerical Weather Prediction Progress Report*. Japan Meteorological Agency, Tokyo, Japan, 194 pp. Online at: http://www.jma.go.jp/jma/jma-eng/jma-center/nwp/outline-nwp/index.htm

Jolliffe, I. T. and Stephenson, D. B. 2003. *Forecast Verification: a Practitioner's Guide In Atmospheric Science*. John Wiley: Chichester, 245 pp.

Kalnay, E., Corazza, M. and Cai, M. 2002. Are bred vectors the same as Lyapunov vectors? In: *Proceeding, AMS Symposium on Observations, Data Assimilation and Probabilistic Prediction*. Orlando, FL, Amer. Meteor. Soc. 173–177.

Keenan, T., Joe, P., Wilson, J., Collier, C., Golding, B. and co-authors. 2003. The Sydney 2000 World Weather Research Programme Forecast Demonstration Project. *Bull. Am. Meteor. Soc.* **84**, 1041–1054.

Koizumi, K., Ishikawa, Y. and Tsuyuki, T. 2005. Assimilation of precipitation data to the JMA mesoscale model with a four-dimensional variational method and its impact on precipitation forecasts. *SOLA* **1**, 45–48.

Kunii, M., Saito, K. and Seko, H. 2010. Mesoscale data assimilation experiment in the WWRP B08RDP. *SOLA* **6**, 33–36.

Kunii, M., Saito, K., Seko, H., Hara, M., Hara, T. and co-authors. 2011. Verifications and intercomparisons of mesoscale ensemble prediction systems in B08RDP. *Tellus* **63A**, 531–549.

Lorenz, E. N. 1995. Predictability: a problem partly solved. In: *Proceedings of The Seminar On Predictability*. Volume I, Reading, Berkshire: ECMWF, 1–18.

Marsigli, C., Boccanera, F., Montani, A. and Paccagnella, T. 2005. The COSMO-LEPS mesoscale ensemble system: validation of the methodology and verification. *Nonlin. Proc. Geophys.* **12**, 527–536.

Miyoshi, T. 2010. NHM-LETKF. *Tech. Rep. MRI* **62**, 159–163.

Miyoshi, T. and Aranami, K. 2006. Applying a four-dimensional local ensemble transform Kalman filter (4D-LETKF) to the JMA nonhydrostatic model (NHM). *SOLA* **2**, 128–131.

Miyoshi, T. and Kunii, M. 2011. The local ensemble transform Kalman filter with the Weather Research and Forecasting model: experiments with real observations. *Pure Appl. Geophys.* doi:10.1007/s00024-011-0373-4.

Miyoshi, T., Yamane, S. and Enomoto, T. 2007. Localizing the error covariance by physical distances within a local ensemble transform Kalman filter (LETKF). *SOLA* **3**, 89–92.

Nutter, P., Stensrud, D. and Xue, M. 2004a. Effects of coarsely resolved and temporally interpolated lateral boundary conditions on the dispersion of limited-area ensemble forecasts. *Mon. Wea. Rev.* **132**, 2358–2377.

Nutter, P., Stensrud, D. and Xue, M. 2004b. Application of lateral boundary condition perturbations to help restore dispersion in limited-area ensemble forecasts. *Mon. Wea. Rev.* **132**, 2378–2390.

Ott, E., Hunt, B. R., Szunyogh, I., Zimin, A. V., Kostelich, E. J.and co-authors. 2004. A local ensemble Kalman filter for atmospheric data assimilation. *Tellus* **56A**, 415–428.

Reynolds, C. and Errico, R. 1999. Convergence of singular vectors toward Lyapunov vectors. *Mon. Wea. Rev.* **127**, 2309–2323.

Saito, K., Fujita, T., Yamada, Y., Ishida, J., Kumagai, Y. and co-authors. 2006. The operational JMA nonhydrostatic mesoscale model. *Mon. Wea. Rev.* **134**, 1266–1298.

Saito, K., Hara, M., Seko, H., Kunii, M. and Yamaguchi, M. 2011. Comparison of initial perturbation methods for the mesoscale ensemble prediction system of the Meteorological Research Institute for the WWRP Beijing 2008 Olympics Research and Development Project (B08RDP). *Tellus* **63A**, 445–467.

Saito, K., Ishida, J., Aranami, K., Hara, T., Segawa, T. and co-authors. 2007. Nonhydrostatic atmospheric models and operational development at JMA. *J. Meteor. Soc. Jpn.* **85B**, 271–304.

Saito, K., Kunii, M., Hara, M., Seko, H., Hara, T. and co-authors. 2010a. WWRP Beijing 2008 Olympics Forecast Demonstration/Research and Development Project (B08FDP/RDP). *Tech. Rep. MRI* **62**, 201 pp. Online at: http://www.mri-jma.go.jp/Publish/Technical/DATA/VOL_62/62_en.html

Saito, K., Kuroda, T., Kunii, M. and Kohno, N. 2010b. Numerical simulations of Myanmar Cyclone Nargis and the associated storm surge Part 2: ensemble prediction. *J. Meteor. Soc. Jpn.* **88**, 547–570.

Seko, H. 2010. Local ensemble transform Kalman filter (LET) method. *Tech. Rep. MRI* **62**, 80–84.

Seko, H., Miyoshi, T., Shoji, Y. and Saito, K. 2011. Data assimilation experiments of precipitable water vapor using the LETKF system: intense rainfall event over Japan 28 July 2008. *Tellus* **63A**, 402–414.

Skamarock, W. C., Klemp, J. B., Dudhia, J., Gill, D. O., Barker, D. M. and co-authors. 2005. *A Description of The Advanced Research WRF Version 2*. NCAR Tech. Note 468+STR. Boulder, CO: National Center for Atmospheric Research, 88 pp.

Torn, R. D., Hakim, G. J. and Snyder, C. 2006. Boundary conditions for limited-area ensemble Kalman filters. *Mon. Wea. Rev.* **134**, 2490–2502.

Vié, B., Nuissier, O. and Ducrocq, V. 2011. Cloud-resolving ensemble simulations of Mediterranean heavy precipitating events: uncertainty on initial conditions and lateral boundary conditions. *Mon. Wea. Rev.* **139**, 403–423.

Wang, X. and Bishop, C. H. 2003. A comparison of breeding and ensemble transform Kalman filter ensemble forecast schemes. *J. Atmos. Sci.* **60**, 1140–1158.

Wang, Y., Bellus, M., Wittmann, C., Steinheimer, M., Weidle, F. and co-authors. 2011. The Central European limited area ensemble forecasting system: ALADIN-LAEF. *Q. J. Roy. Meteor. Soc.* **137**, 483–502.

Warner, T. T., Key, L. E. and Lario, A. M. 1989. Sensitivity of mesoscale-model forecast skill to some initial-data characteristics, data density, data position, analysis procedure and measurement error. *Mon. Wea. Rev.* **117**, 1281–1310.